NeuroResource

Neuron

An Optical Neuron-Astrocyte Proximity Assay at Synaptic Distance Scales

Highlights

- An imaging method was developed to assess astrocyte-synapse proximity
- The method was used to determine the wiring diagram of striatal astrocytes
- Dynamics of striatal astrocyte interactions with excitatory inputs were evaluated
- Resources to track static and dynamic astrocyte-synapse interactions are provided

Authors

J. Christopher Octeau, Hua Chai, Ruotian Jiang, Shivan L. Bonanno, Kelsey C. Martin, Baljit S. Khakh

Correspondence

bkhakh@mednet.ucla.edu

In Brief

The Khakh laboratory and collaborators used state-of-the-art optical and genetic strategies to develop an imaging approach to measure static and dynamic interactions of astrocyte processes with synaptic elements within intact adult brain preparations.

Octeau et al., 2018, Neuron *98*, 49–66
April 4, 2018
https://doi.org/10.1016/j.neuron.2018.03.003

CellPress

Neuron
NeuroResource

An Optical Neuron-Astrocyte Proximity Assay at Synaptic Distance Scales

J. Christopher Octeau,[1] Hua Chai,[1] Ruotian Jiang,[1,4] Shivan L. Bonanno,[3] Kelsey C. Martin,[3] and Baljit S. Khakh[1,2,5,*]
[1]Department of Physiology, David Geffen School of Medicine, University of California Los Angeles, Los Angeles, CA 90095-1751, USA
[2]Department of Neurobiology, David Geffen School of Medicine, University of California Los Angeles, Los Angeles, CA 90095-1751, USA
[3]Department of Biological Chemistry, David Geffen School of Medicine, University of California Los Angeles, Los Angeles, CA 90095-1751, USA
[4]Present address: Tianfu Life Science Park, 901 B2, Translational Neuroscience Center, Department of Anesthesiology, West China Hospital, Sichuan University, Chengdu, Sichuan 610000, China
[5]Lead Contact
*Correspondence: bkhakh@mednet.ucla.edu
https://doi.org/10.1016/j.neuron.2018.03.003

SUMMARY

Astrocytes are complex bushy cells that serve important functions through close contacts between their processes and synapses. However, the spatial interactions and dynamics of astrocyte processes relative to synapses have proven problematic to study in adult living brain tissue. Here, we report a genetically targeted neuron-astrocyte proximity assay (NAPA) to measure astrocyte-synapse spatial interactions within intact brain preparations and at synaptic distance scales. The method exploits resonance energy transfer between extracellularly displayed fluorescent proteins targeted to synapses and astrocyte processes. We validated the method in the striatal microcircuitry following *in vivo* expression. We determined the proximity of striatal astrocyte processes to distinct neuronal input pathways, to D1 and D2 medium spiny neuron synapses, and we evaluated how astrocyte-to-excitatory synapse proximity changed following cortical afferent stimulation, during ischemia and in a model of Huntington's disease. NAPA provides a simple approach to measure astrocyte-synapse spatial interactions in a variety of experimental scenarios.

INTRODUCTION

Astrocytes are abundant glial cells that tile the brain (Khakh and Sofroniew, 2015). Individual astrocytes contain thousands of processes that form well-delineated bushy territories that overlap by as little as ~5% at their boundaries (Bushong et al., 2002, 2004; Halassa et al., 2007; Livet et al., 2007; Wilhelmsson et al., 2006). The finest astrocyte processes are irregular, thin, and sheet-like with dimensions on the tens of nanometer scale and with high surface area to volume ratios (Hama et al., 2004; Haustein et al., 2014; Kasthuri et al., 2015; Kosaka and Hama, 1986). They generally lack organelles, are devoid of GFAP (Kosaka and Hama, 1986; Reeves et al., 2011), but show abundant localized calcium signaling (Bazargani and Attwell, 2016; Shigetomi et al., 2016; Volterra et al., 2014). In terms of morphology, up to 95% of an astrocyte's volume comprises processes (Shigetomi et al., 2013). Extensive and ramified processes are thus a defining feature of astrocytes throughout the CNS.

Individual processes from astrocytes contact blood vessels, neuronal cell bodies, and tens of thousands of synapses (Bushong et al., 2002; Chai et al., 2017; Hama et al., 2004; Kasthuri et al., 2015; Kosaka and Hama, 1986; Ventura and Harris, 1999). In this way, astrocyte processes are positioned to respond to neurotransmitters and to modulate synapses (Khakh and Sofroniew, 2015). Additionally, the close apposition of astrocyte processes to synapses may be necessary for their ability to regulate synapse formation and removal (Allen and Eroglu, 2017). Moreover, the close proximity of astrocyte processes to synapses is important for homeostatic functions such as the regulation of neurotransmitter uptake and ion homeostasis, and for restricting diffusion in the extracellular milieu. Work in the hypothalamus illustrates that the proximity of astrocyte processes to synapses is altered by lactation and dehydration (Oliet et al., 2001; Theodosis et al., 1986). In addition to their roles in the healthy nervous system, astrocytes respond to all forms of brain trauma, infection, injury, and disease, and these changes are also frequently accompanied by altered morphology (Khakh and Sofroniew, 2015). Overall, the literature is replete with examples showing how astrocytes regulate neuronal function. Much of this work invokes or assumes the close apposition of astrocyte processes to synapses, but this has been difficult to directly study at rest, following neuronal activity, or in models of disease. Hence, a fundamental aspect of brain biology, namely the proximity of synapses and astrocyte processes, has remained largely unexplored.

Despite progress with tissue culture systems using postnatal day 6–7 mice (Bernardinelli et al., 2014; Haber et al., 2006), there is currently no way to measure the proximity of astrocyte processes to synapses in adult living brain tissue, to explore differences with respect to genetically defined types of neural inputs, or to determine how proximity changes in mouse models of disease. In addition, astrocytes cultured in serum represent an immature or reactive phenotype (Cahoy et al., 2008), they

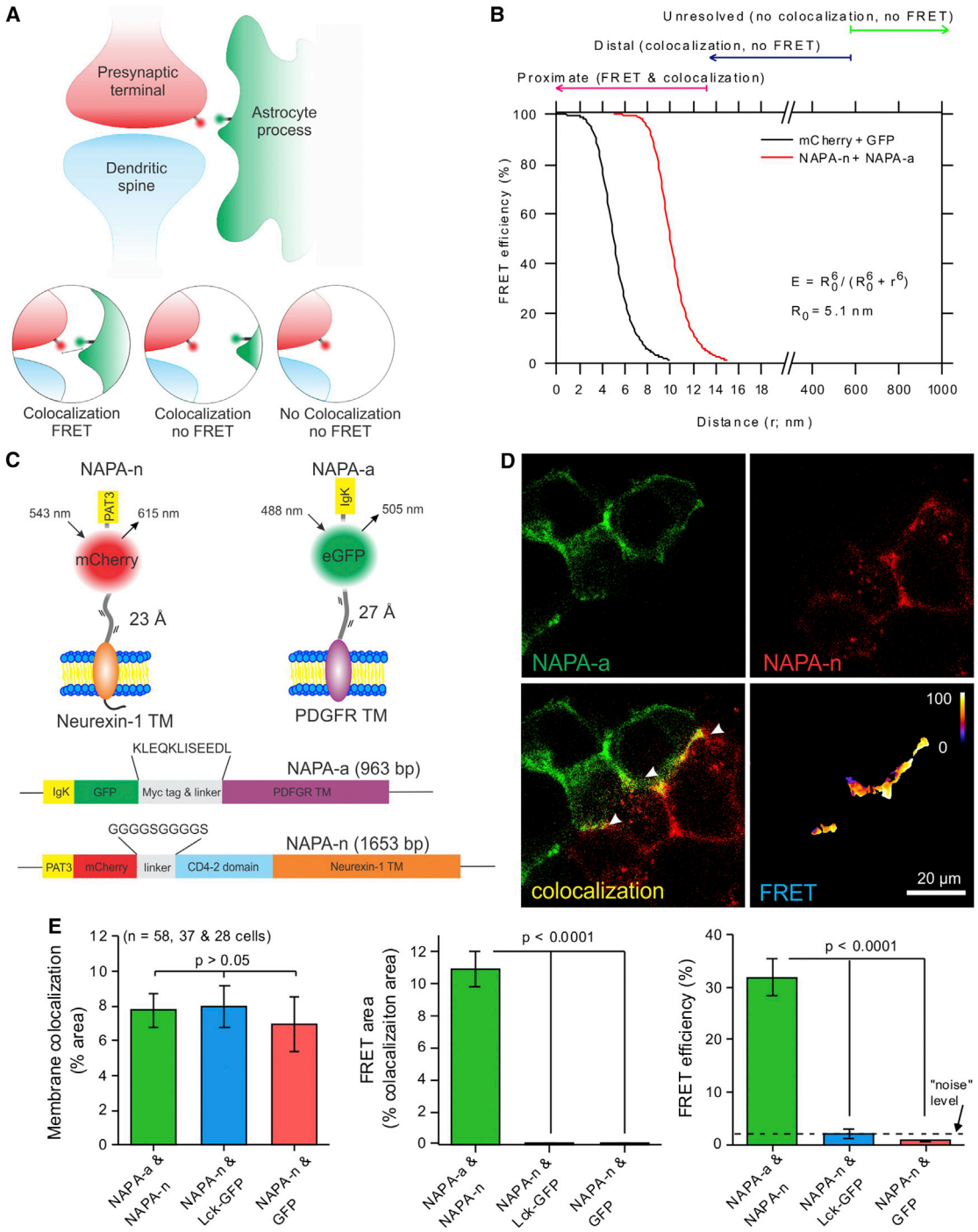

Figure 1. Neuron Astrocyte Proximity Assay to Assess Astrocyte-Synapse Interactions

(A) Diagram of the NAPA assay. Presynaptic terminals are labeled by extracellular, synapse-targeted membrane-tethered mCherry. Fine astrocyte processes opposing these terminals are labeled by extracellular membrane-tethered eGFP. Astrocyte-synapse interactions can be seen at three distance scales.

(B) Graph of intermolecular FRET distances for GFP and mCherry or the intercellular FRET distance for the NAPA-a and NAPA-n probes that contain extended linkers. The arrows above indicate the distance scales over which we can resolve astrocyte synapse interactions with NAPA, corresponding to the inset cartoons in (A).

(C) NAPA-n was targeted to synapses by the Neurexin-1 transmembrane and intracellular C-terminal domains. NAPA-a was targeted to astrocyte processes by the PDGFR transmembrane domain. The lower panels show NAPA-a and NAPA-n cDNA constructs.

(legend continued on next page)

change between the postnatal period and adulthood (Srinivasan et al., 2016; Sun et al., 2013), and their elaborate morphology requires neuronal contacts (Stogsdill et al., 2017), highlighting the need for methods to study adult brain preparations. As such, it remains unclear whether the interactions of astrocyte processes with synapses are dynamic or largely stable in adult brain. We sought to address these issues by developing an approach to measure astrocyte process-to-synapse proximity in live brain preparations for genetically defined cell populations. In this study, we report such an approach. We termed it the neuron-astrocyte proximity assay (NAPA) and used it to assess several open questions.

RESULTS

Neuron-Astrocyte Proximity Assay

Our aim was to develop an imaging-based neuron-astrocyte proximity assay utilizing Förster resonance energy transfer (FRET) between astrocyte processes and presynaptic terminals (Figure 1A). FRET is compatible with live imaging and provides spatial information at synaptic distance scales (Lakowicz, 2006). We also wanted to avoid potential problems associated with irreversible complementation using split GFP and HRP that may stabilize transient interactions (Feinberg et al., 2008; Kim et al., 2011; Martell et al., 2016). We reasoned that appropriate green and red fluorescent proteins (GFPs and RFPs, respectively) capable of FRET such as GFP and mCherry would provide three types of information based on the $\sim 1/r^6$ fall in FRET efficiency as a function of distance.

The point-spread function of our microscope was ~0.6 μm (determined by imaging fluorescent beads). This means that the images shown are diffraction limited at ~0.6 μm x-y resolution. In relation to this, FRET occurs between appropriate molecules when the emission spectrum of the donor overlaps with the absorption spectrum of a cognate acceptor. FRET does not require radiative emission and occurs by dipole-dipole coupling from the donor's excited state. The efficiency of energy transfer between donor and acceptor pairs is determined by their spectral overlap, the quantum yield of the donor, the relative orientation of donor and acceptor dipoles, and the distance between the donors and acceptors (r) with a steep $1/r^6$ relationship, which is summarized in the Förster equation (Figure 1B). Hence, FRET can be used as a spectroscopic ruler to measure proximities, spatial interactions, and under ideal circumstances absolute distances (Stryer, 1978). FRET does not increase the resolution of the imaging system; FRET transduces a near-field interaction into a far-field signal that can be used to assess biological proximity below the diffraction limit. Therefore, the FRET images shown are diffraction limited, but FRET permits inference of proximity several orders of magnitude below the imaged diffraction-limited volumes (Grecco and Verveer, 2011). FRET efficiency reflects energy transfer between the fluorophores and its relationship to proximity by the Förster equation, whereas the FRET area is the area of the ROIs from which FRET was measured.

For NAPA, the distance at which FRET efficiency is 50% (the R_0 for GFP and mCherry) is ~5.1 nm, meaning that FRET would be sensitive to changes over ~10 nm between ~5% and ~95% of its maximum efficiency (Figure 1B). The closest and most proximate interactions between astrocyte processes and synapses where the donor GFP and acceptor mCherry fluorophores undergo energy transfer would be detected as areas of FRET and colocalization between the FPs: these would be at scales of ~10 nm (Figures 1A and 1B). Longer distance scale interactions beyond Förster energy transfer, but at about the diffraction limit of confocal microscopy (~0.6 μm), would be detected as areas of colocalization but would not yield measurable FRET (Figures 1A and 1B). The areas of a labeled astrocyte that contain labeled synapses but displayed neither FRET nor colocalization would indicate spatial interactions that occur over distances of about a micrometer or more, i.e., at distances above the diffraction limit (Figures 1A and 1B).

The presynaptic NAPA component comprised a 29 residue N-terminal nematode β-integrin PAT3 signal peptide, extracellular mCherry, an extracellular domain of ~23 Å length, and the Neurexin-1 transmembrane and cytosolic domains chosen to target presynaptic terminals (Fairless et al., 2008; Kim et al., 2011). We termed the presynaptic neuronal NAPA construct "NAPA-n" (Figure 1C; Figures S1A and S1B). The astrocyte NAPA component comprised a 31 residue N-terminal murine immunoglobulin kappa-chain V-J2-C IgK signal peptide followed by GFP, an extracellular domain of ~27 Å length, and the PDGFR transmembrane domain. We termed the astrocyte NAPA construct "NAPA-a" (Figure 1C; Figures S1A and S1B). The extracellular spacer in NAPA-a was a myc-tag and a small linker, whereas the equivalent spacer in NAPA-n was the CD4-2 domain and a linker (Figure 1C). In the case of NAPA-a, we used different length linkers and found that 12 residues worked reliably. We report data with GFP and mCherry FRET pairs in this study. Figure S1E reports constructs with mNeonGreen and mScarlet.

For testing, we expressed NAPA-a and NAPA-n in HEK293 cells (Figures S1A and S2A–S2F). Both constructs were expressed on the cell edges, and total and cell-surface pools could be detected with antibodies against the FPs in permeabilized and non-permeabilized cells, respectively (Figures S2A–S2C; n = 8 and 14 cells from 3 transfections). Furthermore, acidic pH buffers quenched cell surface fluorescence of NAPA-a or NAPA-n (Figures S2D–S2F; n = 21 cells, 4 transfections). During these experiments, we used two methods to measure FRET between mCherry and GFP: donor dequenching (Figures S3A–S3E; n = 15–31 cells, n = 4 transfections) and sensitized emission (Figures S4A–S4D; n = 40 cells, n = 4 transfections) with mCherry and GFP expressed separately or as a fusion protein (Figures S3

(D) Images of colocalization and FRET in adjoining HEK293 cells that express either the NAPA-a or NAPA-n. Colocalization and FRET occurred at the junctions of cells.

(E) Quantification of colocalization and FRET for NAPA-n and NAPA-a, NAPA-n and Lck-GFP or NAPA-a and cytosolic GFP as assessed by membrane colocalization as a percent of the overlap area (left), FRET area as a percent of colocalization area (middle), and FRET efficiency within the FRET ROIs (right). Mean ± SEM.

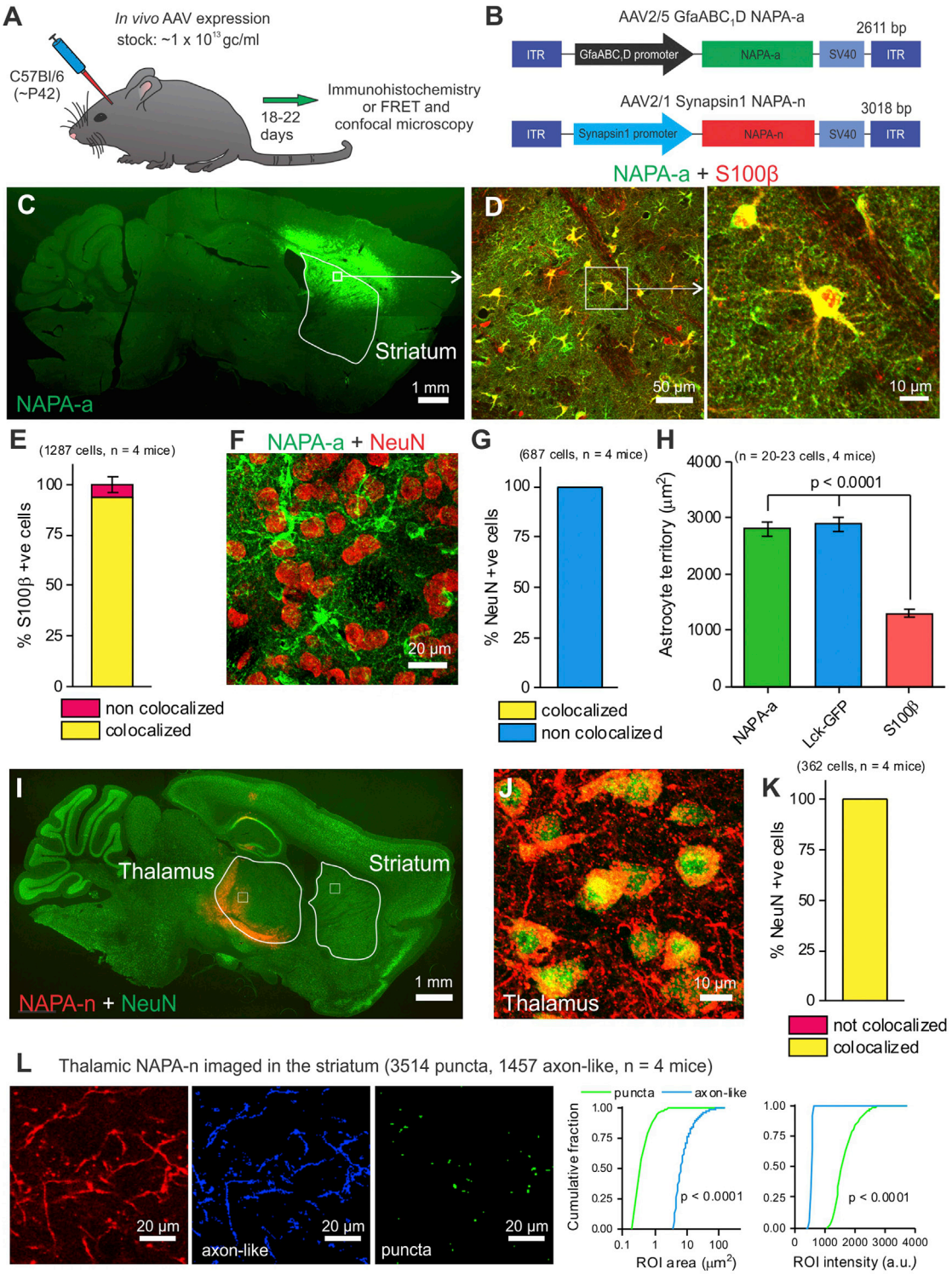

Figure 2. AAVs Selectively Target NAPA Components to Entire Striatal Astrocytes and Presynaptic Terminals

(A) Schematic illustrating the approach.

(B) AAV vectors generated for NAPA-a and NAPA-n, each employing cell-specific promoters.

(C) Representative image showing the distribution of NAPA-a following AAV2/5 microinjections into the dorsolateral striatum.

(D) Representative images of the cellular expression and distribution of NAPA-a in green and the overlap with S100β in red.

(E) Quantification of the percentage of S100β positive cells that colocalized with NAPA-a. Mean ± SEM.

(legend continued on next page)

and S4). The estimates of proximity were similar for the mCherry-GFP fusion construct using either method (Figure S3C, S4C, and S4D). Since sensitized emission FRET does not destroy the FPs, we used this subsequently.

We expressed NAPA-a and NAPA-n separately in HEK293 cells and co-plated the transfected cells. We focused on clusters of cells with juxtaposed NAPA-a- and NAPA-n-expressing cells (Figure 1D). In these, we could image NAPA-a and NAPA-n co-localization at the shared edges and significant FRET in a further subregion (~11%) of the colocalized area (Figure 1E; n = 58 cells, n = 3 transfections). Colocalization was also measured between adjacent cells expressing NAPA-n and Lck-GFP or NAPA-n and cytosolic GFP; however, in cases when the donor FP was intracellular, no FRET was detected (Figure 1E; n = 37 and 28 cells, n = 3 transfections). These data provide strong evidence that cell surface NAPA-a and NAPA-n detect cell-cell contacts by colocalization and that smaller areas representing the closest interactions between plasma membranes are detected by FRET. The controls also define "noise" as ~3% (Figure 1E). NAPA-a and NAPA-n were expressed and localized to distal cell regions in cultured astrocytes and neurons (Figure S4E; n = 3 transfections), permitting their deployment *in vivo*.

Expression of NAPA-a and NAPA-n in Astrocyte Processes and Synapses

The striatum is the largest nucleus within the basal ganglia and serves multiple roles (Graybiel, 2008; Graybiel and Grafton, 2015). Striatal direct D1 and indirect D2 pathway medium spiny neurons (MSNs) integrate glutamatergic inputs from multiple parts of the cortex and thalamus, collateral GABAergic inputs from MSNs (and interneurons), and dense dopaminergic input from the substantia nigra. How astrocytes interact with either D1 or D2 MSNs and the major striatal synaptic inputs is largely unknown, although evidence shows that astrocytes serve important functions (Martín et al., 2015). We used NAPA to determine how striatal astrocytes interact with D1 and D2 MSNs and the major synaptic inputs of the striatum.

For selective expression of NAPA-a within astrocytes *in vivo* (Figures 2A and 2B; Figure S1B), we used AAV2/5 and the astrocyte-specific GfaABC$_1$D promoter that has been extensively characterized (Chai et al., 2017; Jiang et al., 2016; Jiang et al., 2014; Srinivasan et al., 2016; Tong et al., 2014). For selective expression of NAPA-n in neurons we initially used AAV2/1 and the neuron-specific hSynapsin-1 promoter (Figures 2A and 2B; Figure S1B), but we also made FLEX-dependent AAVs and used MSN subtype-specific Cre lines (Atasoy et al., 2008) (Figure S1D). Striatal AAV microinjections resulted in expression of NAPA-a in ~90% of astrocytes, with no detectable expression in neurons (Figures 2C–2G; n = 1,287 astrocytes and 687 neurons, n = 4 mice). NAPA-a was also expressed within entire astrocytes equal in area to those detected by the membrane marker Lck-GFP (Figure 2H; n = 20–23 cells, 4 mice). During initial evaluations, microinjections of NAPA-n AAVs into the thalamus (Figure 2I) resulted in expression of NAPA-n locally within neuron somata (Figures 2J and 2K; 362 cells, n = 4 mice) and also within their projections in processes and bouton-like puncta in the striatum (Figure 2L; n = 4 mice). These punctate structures were significantly smaller (0.53 ± 0.01 versus 11.0 ± 0.44 μm^2; $p < 0.0001$) and brighter (1,663 ± 6 versus 531 ± 1 a.u.; $p < 0.0001$) than the axon-like processes (Figure 2L; n = 3,514 puncta and 1,457 axon-like structures, 4 mice). The bouton-like puncta were also similar in size to synapses labeled with vGLUT2 antibodies in immunohistochemical evaluations (0.48 ± 0.06 μm^2; n = 15,226 puncta, 4 mice; $p < 0.0001$). vGLUT2 labels thalamic presynaptic terminals in the striatum. These data are consistent with trafficking of NAPA-n to presynaptic terminals in the striatum via the neurexin-1 targeting motif. In support, when NAPA-n AAVs were microinjected locally into the cortex or the thalamus, 80% of the resulting puncta in the striatum colocalized with synaptophysin, a marker of presynaptic terminals (Figures S5A–S5B and S5E). Furthermore, following local intrastriatal microinjections of NAPA-n to label MSNs synapses, we found that 80% of puncta were co-labeled with synaptophysin, whereas colocalization with the dendritic marker MAP2 was minimal (Figures S5C–S5E). Thus, astrocyte process and neuronal presynaptic components of NAPA can be expressed selectively in their respective cellular compartments using appropriate AAVs, cell-specific promotors, targeting motifs, and local microinjections (Figure 2). For FRET, we analyzed punctate synaptic-like structures within the striatum.

Astrocytes Interact with Synapses from Major Striatal Inputs

The striatum receives input from the cortex, thalamus, substantia nigra (SNc), as well as local collaterals from MSNs. We characterized astrocyte-synapse proximity for these inputs by using NAPA-a microinjections into the striatum and local NAPA-n microinjections into striatum, motor cortex, thalamus, or SNc. We identified and outlined astrocyte territories using NAPA-a and imaged presynaptic elements using NAPA-n (Figures 3A–3D). We observed robust expression of NAPA-n and NAPA-a and detected clear areas of colocalization and FRET (Figures 3A–3D). The area of colocalization as a percent of the astrocyte territory was ~13%–15% and not significantly different between collateral, cortical, thalamic, and SNc inputs when individually evaluated (Figures 3A–3F; n = 29–30 cells, 4 mice). If one assumes no spatial overlap between distinct types of synapses within the imaged volumes, this suggests that ~57% of a dorsolateral striatal astrocyte's area is equivalently within micrometer scale distances from presynaptic elements from these four pathways.

(F) Representative image of NAPA-a and NeuN.
(G) Quantification of the percentage of NeuN-positive cells that colocalized with NAPA-a. Mean ± SEM.
(H) Size of the astrocyte territory as assessed by IHC, labeled with NAPA-a, Lck-GFP, or S100β. Mean ± SEM.
(I) Representative image of the brain distribution of NAPA-n when microinjected into the rostral intralaminar nucleus of the thalamus.
(J) Representative image of the cellular distribution and overlap of NAPA-a and NeuN.
(K) Quantification of the percentage of NeuN-positive cells that colocalized with NAPA-n. Mean ± SEM.
(L) Representative images and quantification of the thalamostriatal projection labeled by NAPA-n and imaged within the striatum.

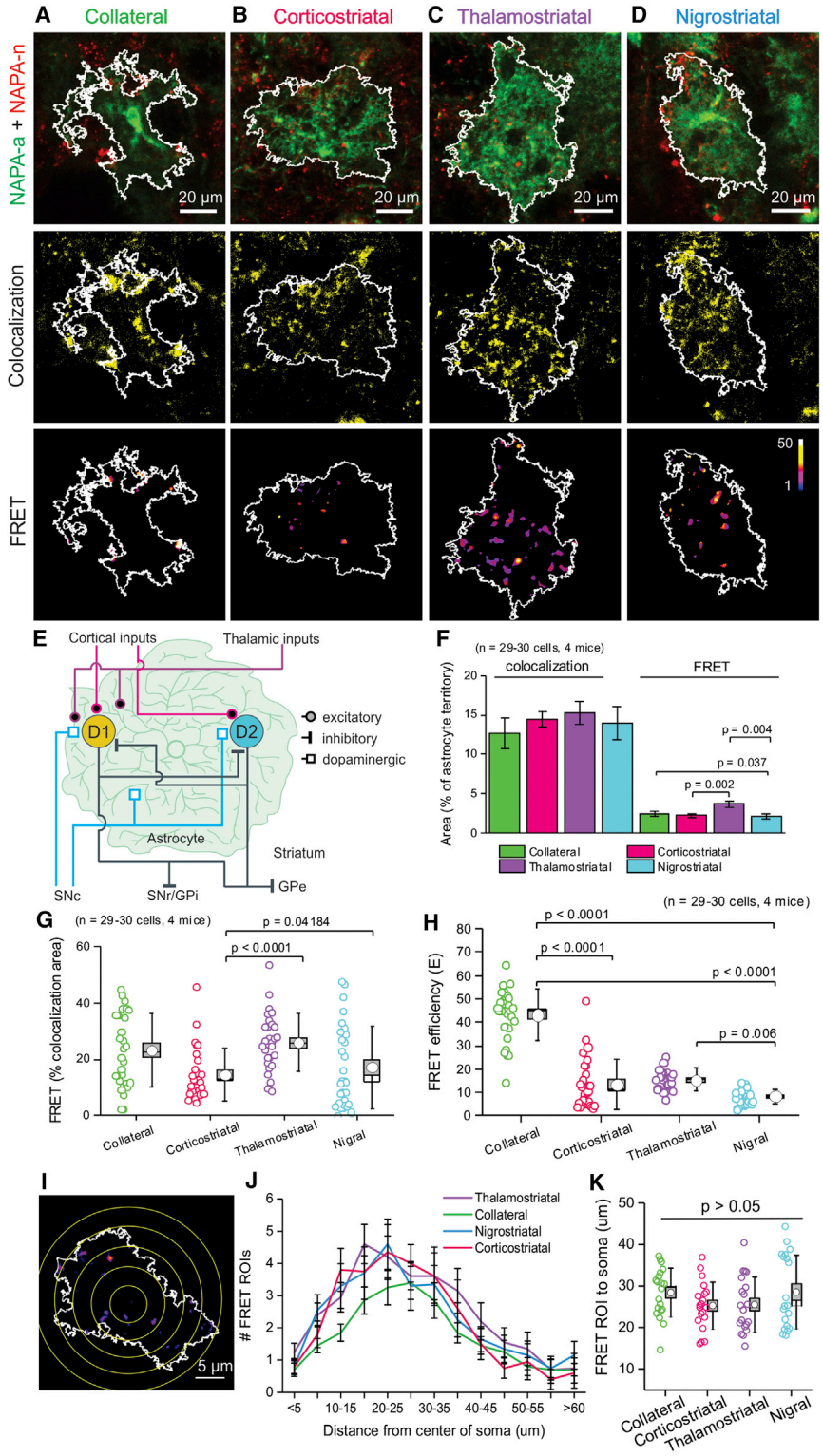

Figure 3. Astrocyte-Synapse Proximity Was Pathway Specific

(A) Representative images of MSN collateral projections expressing NAPA-n and their contacts with astrocyte processes expressing NAPA-a assessed by colocalization and FRET.

(B–D) As in (A), but for corticostriatal (B), thalamostriatal (C), and nigrostriatal (D) inputs. In (A)–(D), the areas of colocalization are shown in yellow, but the areas of FRET are shown on a color scale that reflects FRET efficiency, as shown in the figure.

(E) Diagram of striatal inputs and their plausible contacts with astrocyte processes.

(F) Quantification of striatal input colocalization and FRET with dorsolateral striatal astrocyte processes expressed as a percentage of the astrocyte territory area. Mean ± SEM.

(G) Quantification of the astrocyte area displaying the closest detected astrocyte-synapse interactions as assessed by the area of FRET expressed as a percentage of the total colocalization area per cell. Mean ± SEM: box, SD: whiskers.

(H) Quantification of the relative proximity between astrocyte processes and various striatal inputs as assessed by their FRET efficiency. Mean ± SEM: box, SD: whiskers.

(I and J) Example FRET image of an astrocyte with superimposed circles of increasing diameter (I). Such circles were used to count the number of FRET ROIs as a function of distance in (J). Mean ± SEM: box, SD: whiskers.

(K) Summary plot for the distance of FRET ROIs to the center of the soma. Mean ± SEM: box ± 10%–90% range: whiskers.

Since some overlap is feasible, the value of ~57% is an upper limit. However, while collateral and corticostriatal inputs showed similar areas of FRET, there were significant differences between areas of FRET between collateral and nigrostriatal, corticostriatal, and thalamostriatal, as well as between thalamostriatal and nigrostriatal inputs (Figure 3F; 4 mice per pathway). Thus, the area of FRET was ~2%–4% of the territory for each of these inputs and significantly different between them (Figure 3F; n = 29–30 cells, 4 mice each). These data show that up to ~20% of the colocalized area of an astrocyte's territory contains areas closest to synapses from these distinct inputs, but the underlying FRET signal arises from volumes smaller than the diffraction-limited volumes we imaged. Next, we measured the FRET area as a percent of the colocalization area and found significant differences between different inputs (Figure 3G; n = 29–30 cells, 4 mice). We also measured FRET efficiency and found that the most proximate interactions of striatal astrocytes were with local collaterals and that the interactions with the lowest FRET signal were with SNc inputs (Figure 3H). Excitatory presynaptic elements arising from cortical and thalamic inputs were intermediate and equivalent

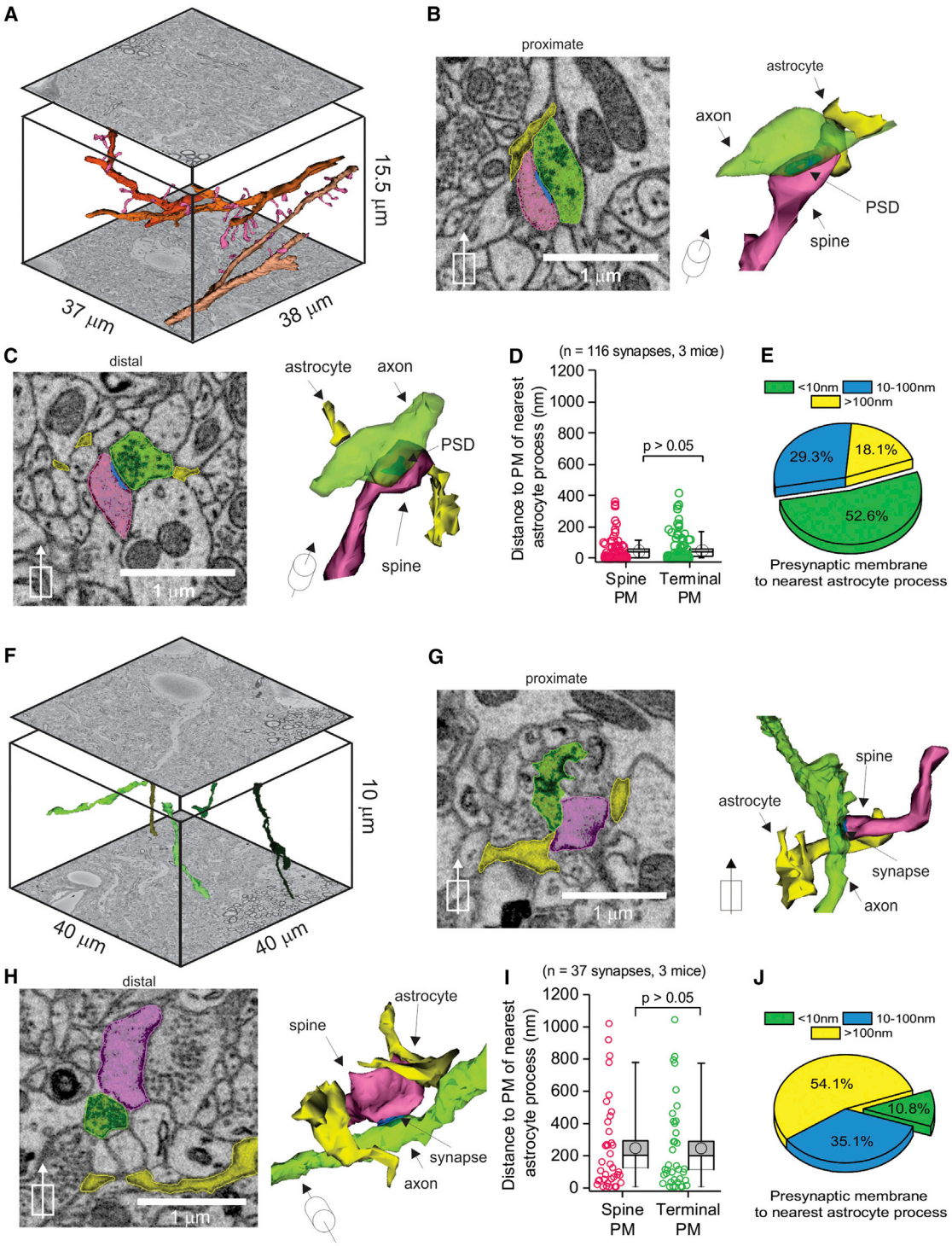

Figure 4. SBF-SEM of Striatal Astrocyte Processes with Presynaptic Terminals and MSN Dendritic Spines

(A) Representative image of three manually traced MSN dendrites within an ~2,180 μm^3 block of the striatum that was scanned by SBF-SEM.

(B) Representative image and three-dimensional reconstruction of a striatal astrocyte process that was closely opposed to the pre- and postsynaptic membranes of an excitatory synapse.

(C) Representative image and three-dimensional reconstruction of a striatal astrocyte process that was more distal to the pre- and postsynaptic membranes of an excitatory synapse.

(D) Quantification of the distance between the nearest astrocyte process and the pre- and post-synaptic membranes of 116 synapses from 3 mice. In the box and whisker plots shown in (D), the mean is shown with a circle, the SEM with the box, the median with a horizontal line, and the 10%–90% range with the whiskers.

(legend continued on next page)

Table 1. Distances of Astrocyte Processes to Synaptic Structures from SBF-SEM

	Excitatory Synapses		TH-Positive Synapses	
	Terminal	Spine	Terminal	Spine
Average (nm)	52	50	248	245
SD	87	141	277	272
SEM	8	13	45	45
Median (nm)	9	7	125	115
Mode (nm)	6.8	6.8	6.8	6.8
n (synapses, mice)	116, 3	116, 3	37, 3	37, 3

The distance of astrocyte processes to terminal membranes of excitatory and TH-positive synapses were significantly different ($p < 0.0001$; unpaired Mann-Whitney test). The distance of astrocyte processes to spine membranes of excitatory and TH-positive synapses were also significantly different ($p < 0.0001$; unpaired Mann-Whitney test).

(Figure 3H). Taken together, these data indicate that striatal astrocytes interact with distinct synaptic inputs in a separable manner. Moreover, on average for any one input a fraction (~30%) of the areas displaying colocalization displayed FRET, implying that astrocytes interact with synapses on micrometer distance scales as seen by colocalization and less frequently in smaller regions at more proximate distance scales, as revealed by FRET. Recapitulating the HEK293 cell control experiments (Figure 1E) in brain preparations, we detected negligible FRET between Lck-GFP expressed in astrocytes and NAPA-n following *in vivo* expression (Figures S6A–S6F; n = 4 and 5 mice per group), indicating that FRET signals reflect extracellular astrocyte-neuron contacts.

To assess the spatial organization of FRET signals within astrocytes for the distinct neuronal inputs, we plotted the number of FRET ROIs as a function of distance from the soma (Figure 3I) and we also measured the average distance from the FRET ROIs to the center of the soma. Irrespective of the type of neuronal input, the number of FRET ROIs peaked at ~25 μm from the soma in areas containing processes (Figure 3J). Moreover, there were no significant differences in the average distance of FRET ROIs to the center of the soma for thalamostriatal, corticostriatal, collateral, and nigrostriatal terminals (Figure 3K; n = 20 cells, 5 mice each). Few FRET ROIs were detected near the somata themselves (Figure 3J). These data indicate that the interactions of astrocyte processes with synapses occur throughout bushy astrocytes.

SBF-SEM of Excitatory and TH-Positive Synapses in Relation to Astrocyte Processes

We used serial block face scanning electron microscopy (SBF-SEM) to examine the proximity between striatal astrocyte processes and presynaptic terminals of asymmetric excitatory synapses that receive input from cortex and thalamus (Frotscher et al., 2014). We followed aspiny dendrites as they emanated from MSN somata and then traced dendritic spines after the first bifurcation in a 15.5 × 37 × 38 μm tissue volume in 80-nm-thick sections with a lateral resolution of ~7 nm (Figure 4A). From such tracings, we identified 116 excitatory synapses from 3 mice. Figures 4B and 4C show representative examples and 3D-reconstructions of astrocyte processes relative to excitatory synapses. We found that the average distance from the pre- or postsynaptic membrane to the nearest astrocyte process's membrane was ~50 nm (Figure 4D; n = 116 synapses, n = 3 mice). We evaluated the distance between astrocyte processes and presynaptic terminals more closely, because there was considerable variability between synapses (Figure 4D), and found ~53% were <10 nm away, i.e., at a distance that would be detected as FRET by NAPA. However, ~47% were between 10 and 400 nm away, i.e., at a distance longer than FRET, but within detection by NAPA colocalization. Overall, the SBF-SEM data support observations with NAPA by showing that astrocyte processes interact with excitatory synapses at multiple scales of distance (Figure 4). The distances at less than ~10 nm when the plasma membranes essentially touch most likely reflect the FRET measurements (Figure 4). The distances greater than ~10 nm are not expected to be detected by FRET but would be seen as colocalization (Figure 4).

We also evaluated the proximity of astrocyte processes to putative dopaminergic terminals that were tyrosine hydroxylase (TH) positive. We traced these structures in a 40 × 40 × 10 μm tissue volume in 80 nm sections with a lateral resolution of ~7 nm (Figure 4F). We identified 37 synapses from 3 mice. Figures 4G–4J show representative examples and 3D reconstructions of astrocyte processes relative to TH-positive synapses. We found that the average distance from the pre- or postsynaptic membrane to the nearest astrocyte process's membrane was ~250 nm (Figure 4I; n = 37 synapses, n = 3 mice, Table 1). We also evaluated the distance between astrocyte processes and presynaptic terminals (Figure 4I) and found ~11% were <10 nm away, i.e., at a distance that would be detected as FRET by NAPA. However, ~89% were between 10 and 1,100 nm away, i.e., at a distance longer than FRET, but largely within detection by NAPA colocalization. Taken together, NAPA and SBF-SEM data suggest that excitatory and TH-positive synapses in the striatum are not ensheathed by astrocyte processes. Instead, astrocyte processes make finer and more variable interactions, consistent with electron microscopy studies of the hippocampus showing that ~57% of synapses are contacted at only ~43% of their synaptic interface by astrocyte processes (Ventura and Harris, 1999; Witcher et al., 2007). The pattern of spatial interactions observed with NAPA whereby astrocytes made more proximate interactions with excitatory synapses as compared to nigral synapses (Figure 3) was consistent with the SBF-SEM data, where a similar and significant trend was observed (Figure 4; Table 1).

(E) Representation of the distances between the nearest astrocyte process and the pre- and post-synaptic membranes, binned to <10 nm, 10–100 nm, and distances that are greater than 100 nm. The data show that striatal astrocytes interact with excitatory synapses at separable distance scales, with around half of the distances being the most proximate at <10 nm.
(F–J) As in (A)–(E) but for TH-positive terminals in relation to astrocyte processes (see Table 1).

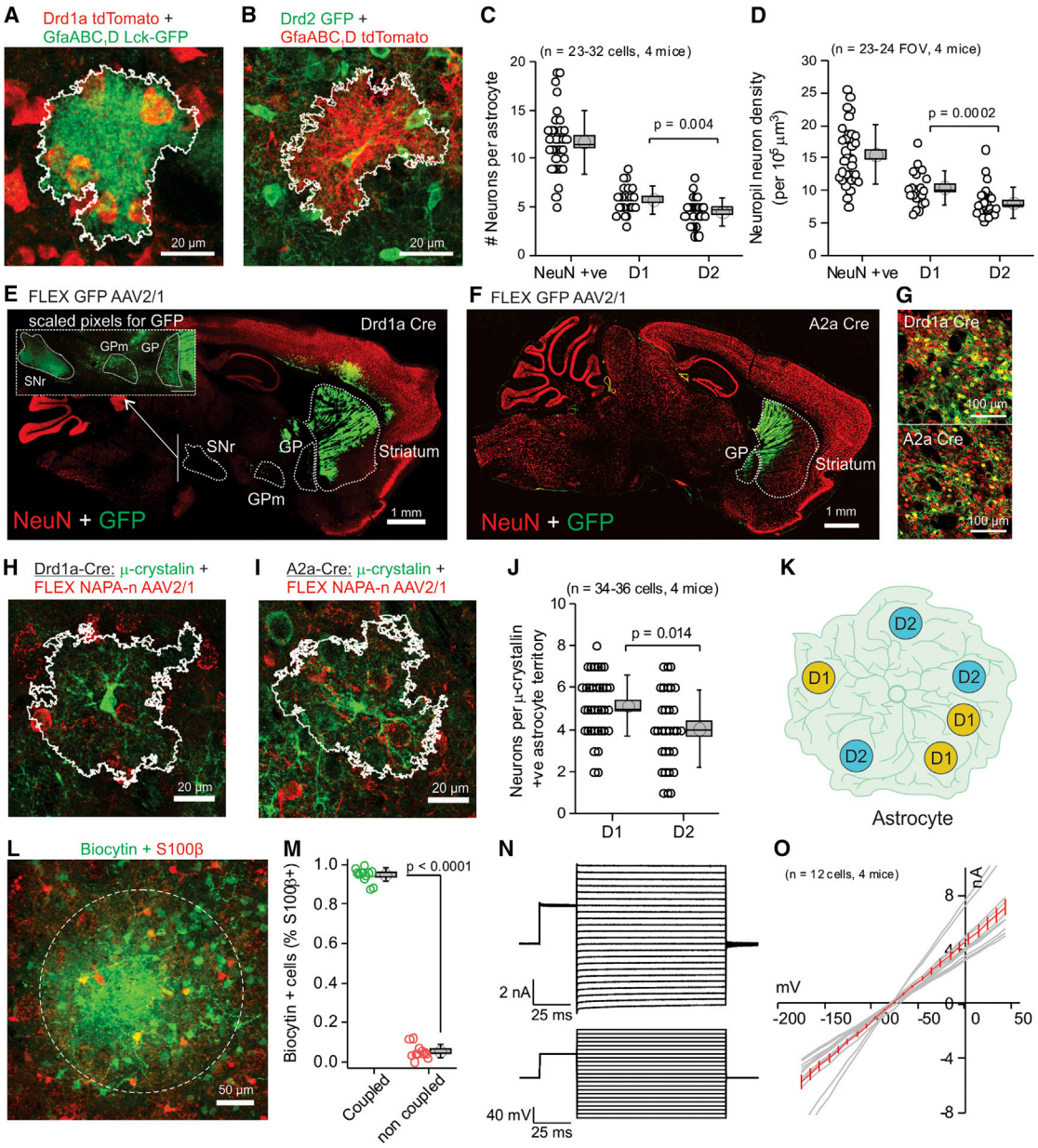

Figure 5. Striatal Astrocytes Contact D1 and D2 MSNs Equivalently

(A) Representative image of a striatal astrocyte that expresses Lck-GFP under the control of the GfaABC$_1$D promoter in BAC D1-tdTomato mice.

(B) Representative image of a striatal astrocyte that expresses tdTomato under the control of the GfaABC$_1$D promoter in BAC D2-GFP mice.

(C) Quantification of the number of neurons within the territory of individual striatal astrocytes as assessed by NeuN staining, D2-GFP or D1-tdTomato labeling, from images such as in (A) and (B). Mean ± SEM: box, SD: whiskers.

(D) Quantification of the density of neurons in the dorsolateral striatum as assessed by NeuN staining, D2-GFP, or D1-tdTomato labeling. Mean ± SEM: box, SD: whiskers.

(E) Image of the brain distribution of GFP when AAV2/1 FLEX CAG GFP was microinjected in the striatum of BAC D1-Cre mice.

(F) Image of the brain distribution of GFP when AAV2/1 FLEX CAG GFP was microinjected in the striatum of BAC A2a-Cre mice. In (E) and (F), the expected projection patterns of D1 and D2 MSNs are seen within the basal ganglia circuit.

(G) Images of the dorsolateral striatum when AAV2/1 FLEX CAG GFP was microinjected in the striatum of either BAC D1-Cre or BAC A2a-Cre mice, as in (E) and (F).

(H) Representative image of a µ-crystallin positive dorsolateral striatal astrocyte in BAC D1-Cre mouse that had been microinjected with AAV2/1 FLEX NAPA-n.

(I) Image of a µ-crystallin positive dorsolateral striatal astrocyte in BAC A2a-Cre mouse that had been microinjected with AAV2/1 FLEX NAPA-n.

(J) Quantification of the number of neurons per µ-crystallin-positive striatal astrocyte in BAC D1-Cre and BAC A2a-Cre mice, as in (H) and (I). Mean ± SEM: box, SD: whiskers.

(legend continued on next page)

Spatial Interactions of Striatal Astrocytes with D1 and D2 MSN Somata and Synapses

We used NAPA to explore whether striatal astrocytes form preferential relationships with either D1 or D2 MSNs. We labeled all neurons with NeuN and used Drd1a-tdTomato and Drd2-GFP reporter lines to identify D1 and D2 MSNs (Ade et al., 2011; Thibault et al., 2013). We found that a striatal astrocyte's territory included ~11 NeuN-positive cells, of which on average ~6 were D1 MSNs and ~5 were D2 MSNs (Figures 5A–5C). Although the number of D1 MSNs per astrocyte was significantly greater than D2 MSNs (Figures 5A–5C; $p = 0.004$), these differences were small and in accord with the density of D1 and D2 MSNs per unit volume (Figure 5D; n = 23–32 fields-of-view, n = 4 mice). Recent data show that μ-crystallin (μ-cry) defines an ~40% subpopulation of dorsolateral striatal astrocytes (Chai et al., 2017). We explored the possibility that this subpopulation may interact preferentially with D1 or D2 MSNs (Figures 5A–5C). To test for this, we microinjected FLEX-dependent GFP or NAPA-n AAVs into Drd1a or A2a Cre mice (Gong et al., 2007) to selectively label D1 or D2 MSNs with GFP (Figures 5E–5G; Figures S6G–S6I) and then immunostained for μ-cry-positive astrocytes (Figures 5H and 5I). We found that although the number of D1 MSNs was higher than D2 MSNs per μ-cry-positive territory, this difference was in proportion to the overall number of D1 to D2 MSNs in the striatum (Figures 5J and 5K).

Astrocytes couple via intercellular gap junctions to form extensive networks of coupled cells. We next determined whether striatal astrocytes coupled to all nearby astrocytes or to a subpopulation, which may then interact preferentially with D1 or D2 MSNs, i.e., do subnetworks of coupled astrocytes exist? However, we found that intracellular biocytin dialysis of striatal astrocytes displaying typical passive properties resulted in the spread of the intracellular tracer to 98% of S100β-positive astrocytes (Figures 5L–5O; n = 12 slices, 4 mice).

Next, we used NAPA to determine whether striatal astrocytes interacted preferentially with synapses emanating from D1 and D2 MSNs within the striatum (Figure 6). We thus made FLEX-dependent AAV2/1 (Figure S1D) to express NAPA-n in a Cre-dependent manner within the striata of either Drd1a or A2a-cre mice. The astrocyte territories and the areas of colocalization and FRET were similar for astrocytes interacting with D1 and D2 MSNs (Figures 6A–6D; n = 24–25 cells, n = 4 mice each). Moreover, the number of ROIs displaying colocalization (Figure 6E) and FRET per astrocyte (Figure 6F), the FRET efficiency (Figure 6G), and the area of FRET as a percentage of the colocalized area (Figure 6H) were not significantly different between D1 and D2 MSNs ($p > 0.05$ in each case). Thus, our evaluations using AAVs, μ-cry, D1 and D2 reporter mice, and Cre lines along with somatic and synapse level evaluations with NAPA failed to find strong evidence to suggest that striatal astrocytes interact preferentially with either D1 or D2 MSNs at an anatomical level (Figure 5K). Our data are consistent with the model that astrocytes interact broadly with D1 and D2 MSNs.

Astrocyte Spatial Interactions with Cortical Synapses: Effect of EFS and OGD

We used selective electrical field stimulation (EFS) of cortical afferents in parasagittal brain slices to study the influence of corticostriatal synaptic transmission on astrocyte spatial interactions with cortical nerve terminals. Since striatal astrocytes do not respond reliably to single APs (Chai et al., 2017; Jiang et al., 2016), we applied trains of stimuli to evoke action potentials (APs) in cortical axons (10 s at 10 Hz, 4 mA). EFS evoked clear EPSCs onto all MSNs ~200 μm from the stimulating site (Figures 7A–7C; n = 12 MSNs, 4 mice) and resulted in iGluSnFR glutamate signals onto astrocytes (Marvin et al., 2013): these were potentiated by blocking glutamate transporters with TBOA (1 μM) and blocked by TTX (500 nM) (Figures 7D and 7E). Furthermore, EFS resulted in localized Ca^{2+} signals detected in astrocytes expressing Lck-GCaMP6f (Srinivasan et al., 2016). These signals were potentiated by TBOA and blocked by TTX (Figure 7F). The EFS conditions employed did not cause significant change in astrocyte territory area: following EFS, the territory area was 99% ± 6% of its pre EFS value, which was 3,151 ± 137 μm^2 ($p > 0.05$, n = 15 cells, 4 mice). Similarly, in the presence of TTX, the territory area was 99% ± 7% of its pre EFS value, which was 2,996 ± 175 μm^2 ($p > 0.05$, n = 20 cells, 4 mice).

We next determined whether EFS-evoked synaptic activity altered astrocyte-synapse interactions on the minutes timescale. We monitored FRET and colocalization between striatal astrocyte NAPA-a and NAPA-n (following cortical microinjections of NAPA-n). First, we found that neither FRET efficiency, FRET area, nor colocalization area were affected by TTX, indicating that ongoing AP firing does not contribute measurably to astrocyte-synapse interactions (Figures 7G–7J; n = 14–18 cells, 4 mice). Second, we found that EFS failed to alter FRET efficiency, FRET area, or colocalization area for up to 10 min after EFS (Figures 7G–7J). Third, the data were essentially identical for EFS whether the experiments were performed in the presence or absence of TTX, which further argues that AP firing does not alter spatial interactions between astrocyte processes and synapses (Figures 7G–7J). However, it remained possible that individual ROIs may have changed in FRET efficiency. To address this, we plotted the FRET efficiency over time for control and +TTX conditions (Figures 7K and 7L) and found no time-dependent changes in either group for the individual traces or from the average plots (Figure 7M). Our data suggest that astrocyte-synapse interactions in the corticostriatal pathway are stable and do not show a high degree of spontaneous or AP-dependent dynamics.

(K) Schematic depicting the somata of both D1 or D2 MSNs within the territory of an individual striatal astrocyte, which our data indicate interact equivalently with both cell types.

(L) Image showing biocytin labeling of coupled astrocytes in the striatum, when a single striatal astrocyte was dialyzed with biocytin for 30 min.

(M) Quantification of the percentage of S100β-positive cells that were also biocytin positive in the striatum following intracellular dialysis of a single astrocyte: these are shown as the coupled cells. Mean ± SEM: box, SD: whiskers.

(N) Representative current waveforms for a striatal astrocyte in response to stepwise changes membrane potential.

(O) Average current-voltage relationship (I/V curve) of dorsolateral striatal astrocytes.

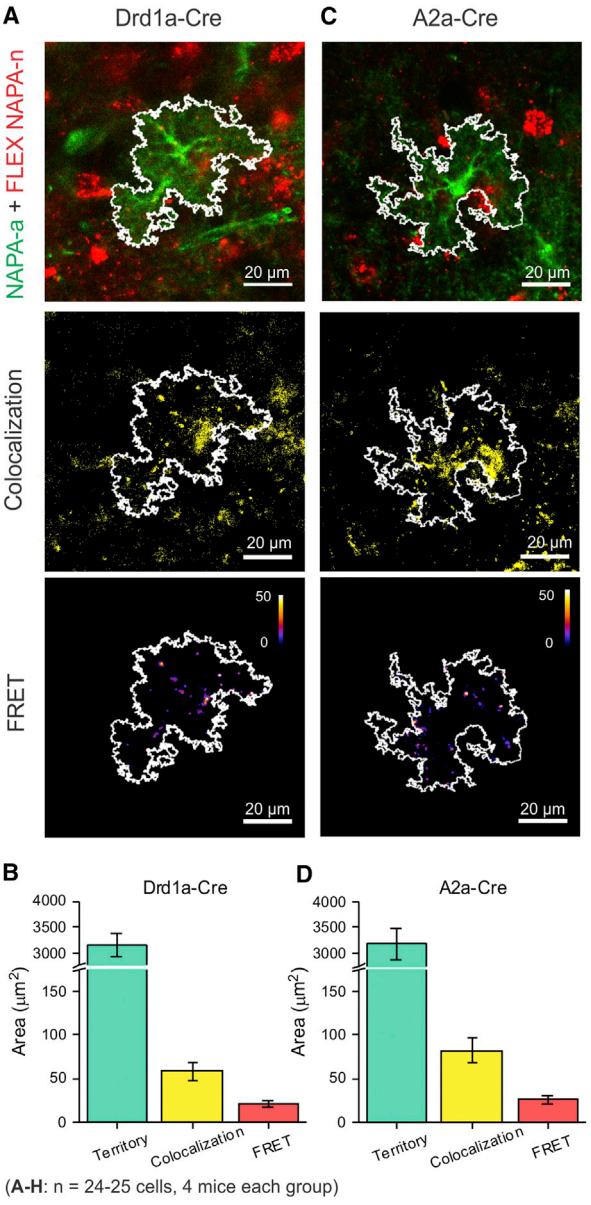

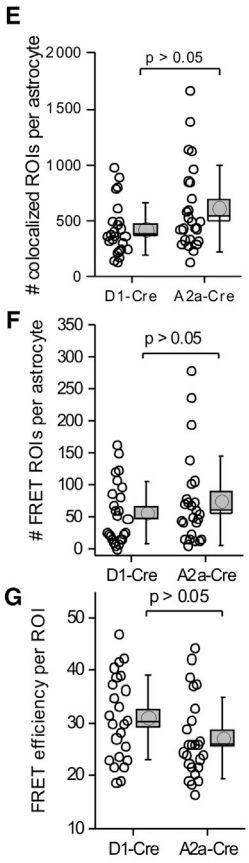

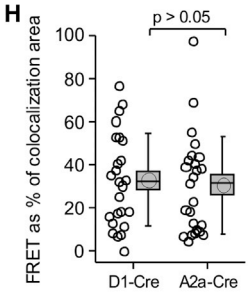

Figure 6. NAPA Analyses of the Contacts between D1 and D2 MSN Collaterals and Striatal Astrocyte Processes

(A) Representative images of NAPA-n expression within D1 MSN collaterals and their contacts with astrocyte processes expressing NAPA-a.

(B) Quantification of the area of the striatal astrocyte territory occupied by colocalized (yellow bar) and FRET ROIs (red bar) for D1 MSNs. Mean ± SEM.

(C) Representative images of NAPA-n expression within D2 MSN collaterals and their contacts with astrocyte processes expressing NAPA-a.

(D) Quantification of the area of the striatal astrocyte territory occupied by colocalized (yellow bar) and FRET ROIs (red bar) for D2 MSNs. Mean ± SEM.

(E) The number of colocalized ROIs for D1 and D2 collaterals in the territory of striatal astrocytes. Mean ± SEM: box, SD: whiskers.

(F) The number of FRET ROIs for D1 and D2 collaterals in the territory of striatal astrocytes. Mean ± SEM: box, SD: whiskers.

(G) The FRET efficiency of ROIs for either D1 projections or D2 collaterals within the territory of striatal astrocytes. Mean ± SEM: box, SD: whiskers.

(H) Quantification of the areas displaying FRET as a percent of total area of colocalization for either D1 or D2 MSNs. Mean ± SEM: box, SD: whiskers.

We next used oxygen-glucose deprivation (OGD) to determine how striatal astrocyte-synapse spatial interactions were affected in this brain slice model of ischemic stroke. OGD applications depolarized MSNs from −73 ± 1 to −12 ± 7 mV (n = 15 cells, 5 mice) and astrocytes from −84 ± 1 to −46 ± 12 mV (n = 7 cells, n = 3 mice) within ~15 min. Under these conditions, OGD also significantly increased the astrocyte territory area by ~20% from 2,778 ± 265 µm^2 (Figures 8A and 8B; n = 12 cells, 5 mice). Furthermore, when astrocyte territory area increases reached steady state, the areas of colocalization and FRET were significantly increased by 50% and 100%, respectively (Figure 8C; n = 12 cells, 5 mice). However, the FRET efficiency did not increase, but in contrast displayed a subtle decrease by ~10% (Figure 8C; n = 12 cells, 5 mice). Taken together, these data show that OGD-evoked astrocyte shape changes are associated with increased FRET and colocalization areas, but not FRET efficiency. The relative stability of FRET efficiency during EFS and OGD suggests that the most proximate astrocyte-synapse interactions are remarkably stable in the striatum, even during OGD-evoked swelling. Our data imply the existence of molecular mechanisms that may stably "bind" astrocyte processes to synapses. RNA-seq data suggest such mechanisms could involve neurexin-neuroligin interactions (Chai et al., 2017; Srinivasan et al., 2016) and recent studies have demonstrated such roles (Stogsdill et al., 2017).

Altered Astrocyte-Synapse Proximity in Huntington's Disease Model Mice

Astrocyte biology is altered in Huntington's disease (HD) and in HD mouse models. For example, recent studies show altered astrocyte-mediated K^+ and glutamate homeostasis in the R6/2 mouse model (Jiang et al., 2016; Khakh et al., 2017; Tong et al., 2014). We next evaluated whether astrocyte morphology and spatial interactions with synapses were changed in R6/2 HD model mice. We began by examining GFAP expression in the striatum of R6/2 and WT mice at ~P70 (Figures S7A–S7C; n = 28–32 cells, 3 mice) and found similarly low levels in both genotypes throughout the dorsolateral striatum (Mangiarini et al.,

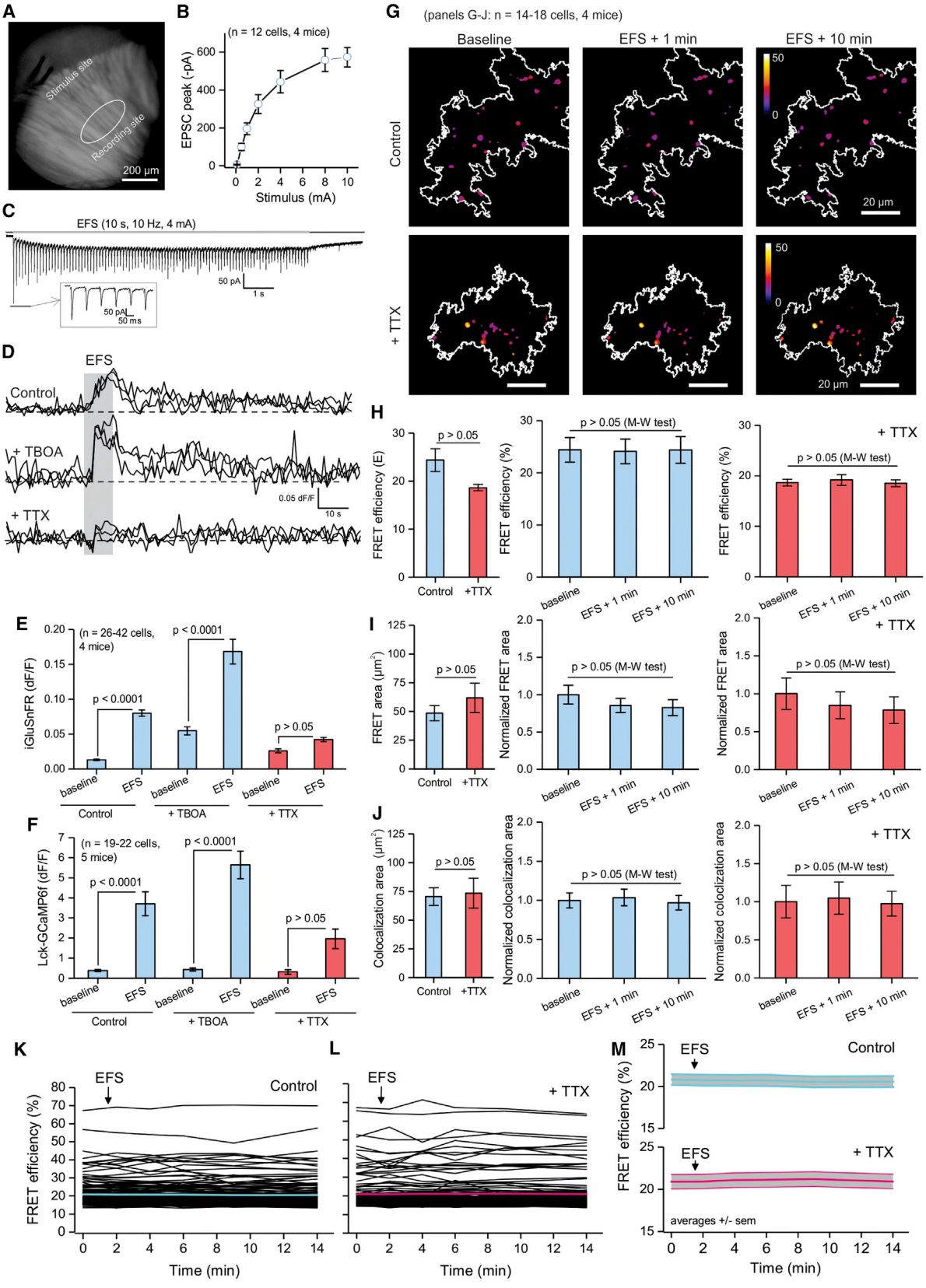

(legend on next page)

1996; Tong et al., 2014). These observations were confirmed by quantifying GFAP areas, GFAP intensity, and the per-cell GFAP area (Figures S7A and S7B), as well as by performing Sholl analysis of GFAP morphology at a distance of 25 μm from the soma (Figure S7C). In all cases, we found no significant differences between R6/2 and WT mice, confirming past reports that R6/2 mice do not display overt astrogliosis at ~P70 (Khakh et al., 2017).

Next, we examined astrocyte territory sizes in WT and R6/2 mice with NAPA-a. We found no significant differences in the size of the astrocyte somata between WT and R6/2 mice, but the territory area was significantly smaller in R6/2 mice (Figures 8D and 8E; $p < 0.0001$ n = 77 cells, 4 mice each). To verify these measurements, we used intracellular lucifer yellow iontophoresis in lightly fixed tissue combined with confocal imaging and 3D reconstructions. These evaluations confirmed the NAPA-a data showing that astrocytes from R6/2 mice displayed significantly smaller territories (Figures 8F and 8G; $p = 0.002$, n = 16–18 cells, 4 mice), illustrating the limitations of GFAP for studying astrocyte morphology and emphasizing the utility of cell surface NAPA-a. We next used NAPA to measure the proximity of astrocyte processes to cortical and thalamic inputs (Figure 8H). In the case of cortical inputs, we measured no change in colocalization area but recorded significantly smaller areas with FRET. In these areas, FRET efficiency was significantly higher in R6/2 mice (Figure 8I; n = 37–40 cells, 4 mice). In contrast, for thalamic inputs we measured significantly greater colocalization and FRET (both area and efficiency) between astrocyte processes and thalamic inputs in the R6/2 mice (Figure 8J; n = 37–40 cells, 5 mice). These data suggest that the number of the most proximate astrocyte processes to cortical inputs decreased in symptomatic R6/2 mice, whereas this parameter increased for thalamic inputs. Another explanation could be that the proximate cortical interactions were maintained, but those located more distally were lost. Irrespectively, our data emphasize the utility of NAPA to reveal pathway specific changes of astrocyte-synapse interactions for the two major excitatory pathways of the striatum in HD model mice. Interestingly, the changes in cortical and thalamic pathways occurred before loss of cortical and thalamic presynaptic vGLUT1 and vGLUT2 immunostaining (Figure S8). Hence, the use of NAPA shows that astrocyte dysfunction and process withdrawal from excitatory synapses precede excitatory synapse loss in HD model mice (Khakh et al., 2017). Together with the known loss of Glt1, the altered spatial interactions of astrocyte processes with excitatory synapses represents an early dysfunction in HD model mice that occurs in the absence of overt astrogliosis. Diminished astrocytic homeostatic support could be a trigger for synapse loss.

DISCUSSION

We developed a genetically encoded FRET-based imaging approach called NAPA, which permits non-invasive evaluation of how astrocyte processes interact spatially with distinct neural circuit pathways on distance scales relevant to synapses. NAPA permits evaluation of individual pathways one at a time in relation to astrocytes but could be expanded with additional FRET pairs.

There is mounting evidence that the spatial interactions of astrocytes with neurons and synapses are important and malleable. Cajal presented and abandoned an early hypothesis that neuroglia were capable of lengthening their appendages and intervening between neuronal connections, which would lead to inactivity in the latter (DeFelipe and Jones, 1988). In this scenario, the neurons would regain activity when they would enter into free contact with each other upon retraction of the neuroglial processes. While there is no evidence to support the idea that astrocyte processes physically intervene to inactivate synapses, recent studies show that astrocyte processes may move relative to synapses with potentially important functional sequelae such as synapse formation and removal (Allen and Eroglu, 2017). However, three issues have hampered progress. First, the underlying biology is remarkably complex: a single astrocyte contains tens of thousands of synapses within its territory and astrocyte processes are extremely thin and branched such that they could not be traced reliably in state-of-the-art scanning electron microscopy projects (Kasthuri et al., 2015). Second, protoplasmic astrocytes are not polarized and exhibit largely equivalent, bushy territories when assessed by light or electron microscopy (Khakh and Sofroniew, 2015), which makes it problematic to study interactions of specific structures in relation to neural inputs. Thus, we are not aware of any known structures within astrocyte processes that are akin to presynaptic active zones or postsynaptic densities that would suggest a high degree of synaptic specialization. Third, a way to measure spatial interactions of astrocyte processes with synapses at appropriate scales in living brain tissue from adult vertebrates has not been available.

Inputs to Striatal Astrocytes

We assessed differences between presynaptic terminals from the major neural pathways to the striatum and found preferential interactions between astrocytes and terminals from these discrete origins. For example, astrocytes make greater areas of close contact with thalamostriatal projections than with corticostriatal projections. However, certain interactions have no substantive anatomical differences in terms of their astrocyte-synapse proximity, such as D1 and D2 MSN collateral synapses

Figure 7. Electrical Field Stimulation of Cortical Axons and Effects on Astrocyte Spatial Interactions with Corticostriatal Synapses

(A) Photograph of a parasagittal brain slice to show the location of the imaging site in relation to electrical field stimulation (EFS).
(B) Input-output curve for evoked EPSCs onto MSNs. Mean ± SEM.
(C) Representative trace for evoked EPSCs recorded from MSNs during a train of EFS.
(D) Representative traces for iGluSnFR signals measured from striatal astrocytes during cortical stimulation.
(E) Average data for experiments such as those in (D). Mean ± SEM.
(F) Average data for experiments such as those in (D) but with calcium imaging using Lck-GCaMP6f. Mean ± SEM.
(G) Representative images showing astrocyte territories and FRET ROIs for the indicated conditions.
(H–J) Averaged data for experiments such those shown in (G), reporting FRET efficiencies (H), FRET ROI areas (I), and the areas of colocalization (J). Mean ± SEM.
(K–M) Individual and average data for FRET efficiency over time before and after EFS under control conditions and in the presence of TTX. Mean ± SEM.

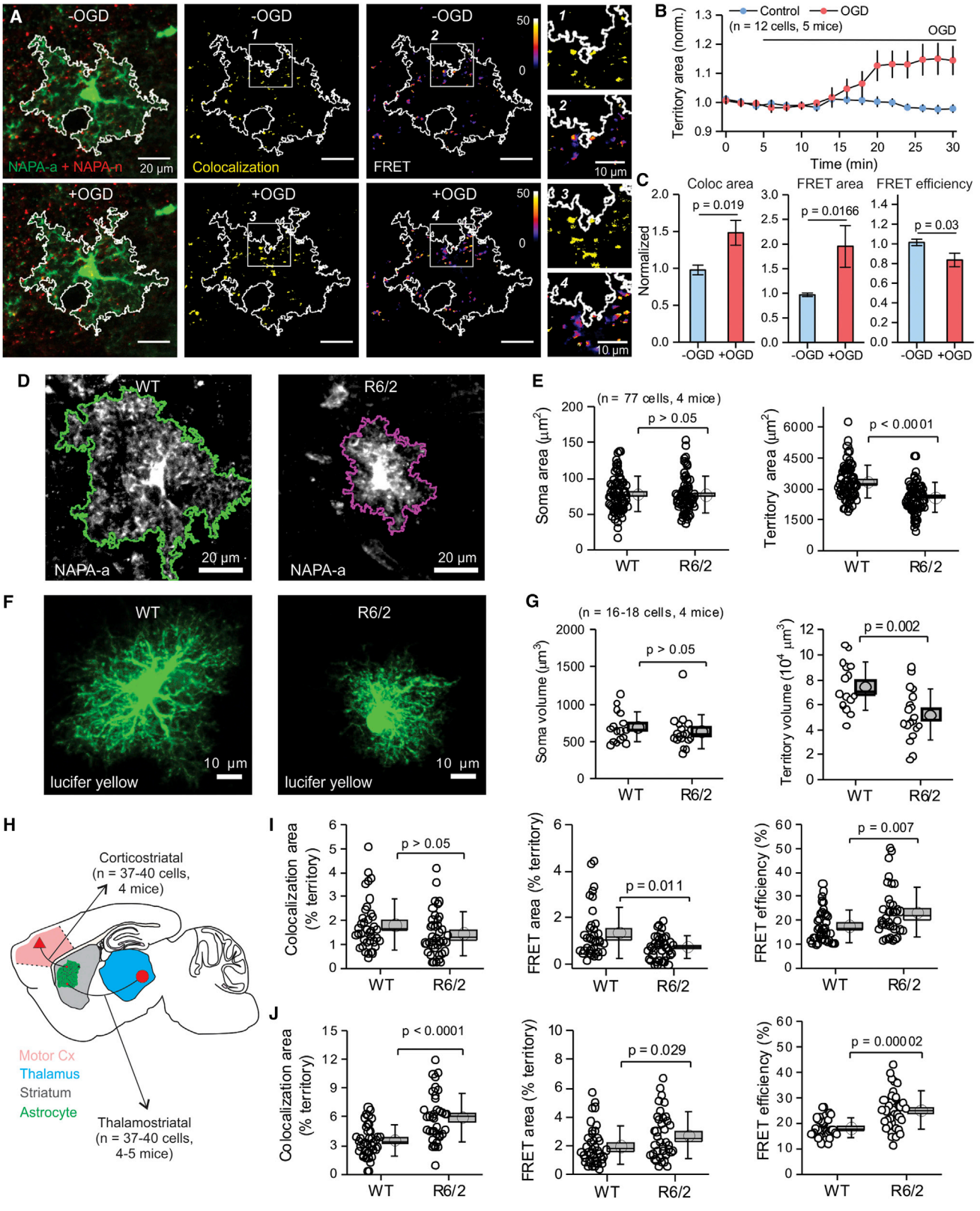

(legend on next page)

or their somata. This result implies that astrocyte-mediated homotypic signaling (i.e., D1 to D1 and not D1 to D2) via Ca^{2+}-dependent glutamate release (Martín et al., 2015) was not reflected by anatomical differences detected by NAPA. Taken together, our data are consistent with the model that striatal astrocytes sample D1 and D2 MSNs largely equivalently and in accord with their regional density, which implies that they may regulate MSN synapses and neurons based on volumetric criteria rather than highly specific interactions. Our data provide connectome-type data for astrocytes, but it is important to recognize that the relationship between connection and function is not fully delineated; functional evaluations are needed.

We found that the most proximate astrocyte process interactions with cortical synapses assessed by FRET efficiency were stable during imaging sessions of up to 30 min, during EFS, and following OGD. Interestingly, motile astrocyte processes have not been reported during *in vivo* calcium imaging studies (Nimmerjahn and Bergles, 2015; Shigetomi et al., 2016), which is consistent with our observations that astrocyte processes are stable. In contrast, microglia are known to be highly dynamic cells and their motility is easily observed (Schafer et al., 2013). We propose that comparatively stable astrocyte interactions with synapses may provide the anatomical substrate (i.e., "track") on which microglial processes move in order to survey synapses (Schafer et al., 2013). This possibility could be explored by using NAPA along with a third color for microglia. Our data also show that astrocyte spatial interactions with the major excitatory inputs to the striatum are altered in Huntington's disease model mice, which recalls work in the hypothalamus (Oliet et al., 2001; Theodosis et al., 1986). The data suggest that astrocyte processes withdraw from corticostriatal synapses in HD model mice at early stages not associated with synapse loss or strong astrogliosis. These changes accompany altered synaptic and astrocyte function (Khakh et al., 2017). This finding suggests that restoring astrocyte proximity, glutamate buffering, and potassium homeostasis in relation to corticostriatal inputs may be desirable in HD.

Considerations when Interpreting FRET and Future Developments

FRET reflects that donor and acceptor FPs on astrocyte processes and presynaptic elements of synapses were within proximity to undergo energy transfer, which in our case has a R_0 of ~5.1 nm and a range of ~10 nm. Conversely, the absence of FRET indicates that astrocyte processes and synapses were beyond this proximity. However, we would be remiss if we failed to discuss photophysical uncertainties and assumptions. First, R_0 includes terms for the donor quantum efficiency (φ_D), the solvent refractive index (n), overlap of the donor emission and acceptor absorption spectra (J_{DA}), and the orientation factor (κ^2) (see Data Analyses). Importantly, the term for the fluorophore dipole orientation factor (κ^2) at 2/3 assumes random orientations of the FPs (Lakowicz, 2006). Given that we do not know the relative orientation of the FPs on astrocyte processes and synapses, assuming a κ^2 value of 2/3 seems parsimonious (Grecco and Verveer, 2011; Lakowicz, 2006). Second, in the case of synapses, we do not know the absolute amount of donor to acceptor FPs: our data represent an average from different donor/acceptor ratios (Khakh et al., 2005; Srinivasan et al., 2012). Third, one expects asymmetry at the synaptic scale in how astrocyte processes interact with synapses and this may vary across synapses even of the same type. Fourth, assuming genuine FRET occurs in a small subdiffraction volume between astrocytes processes and synapses, additional donor and acceptor fluorophores in the same volume will decrease apparent FRET. This type of "bystander" contribution would occur if, for example, there were nearby donor or acceptor bearing astrocyte processes and terminals within the imaged volumes. However, FRET is most reliable when the donor/acceptor ratios are between ~0.1 and ~10 (Berney and Danuser, 2003). This is the case in our experiments for ~90% of the FRET ROIs and we interpret this to indicate that bystander contributions to true FRET are small. Appropriate assessments will be needed in future studies and bystander contributions may be more significant for large synapses that contain multiple active zones in a single large terminal with astrocyte processes at the perimeter. The aforementioned aspects are important to consider, but they do not vitiate the findings that FRET was robust and measurable with NAPA, in accord with SBF-SEM data, distinct for the striatal inputs examined and altered in two disease-related models (OGD and HD). The unknowns in FRET may be resolved in the future with the advent of methods that permit correlated FRET and SBF-SEM of the same single synapses as well as with the development of a framework to experimentally measure and theoretically evaluate complex structural geometries and donor/acceptor ratios.

What Experiments Will NAPA Enable?

First, NAPA can be used to explore how astrocyte-synapse interactions change in response to action potential firing in distinct neural circuit pathways, as we have done for striatum. The underlying synaptic mechanisms can be explored using

Figure 8. Altered Proximity during OGD and in R6/2 Huntington's Disease Model Mice

(A) Representative images for astrocyte territory areas, colocalization and FRET under control conditions and in OGD. The insets (1 to 4) are blown up to the right.

(B) Time course for how astrocyte territory area increased in OGD (data normalized to –OGD). Mean ± SEM.

(C) Summary bar graphs for colocalization area, FRET area, and FRET efficiency under control conditions. Mean ± SEM.

(D) Representative images of dorsolateral striatal astrocytes expressing NAPA-a in either WT or R6/2 mice.

(E) Area of dorsolateral striatal astrocytes as assessed by a flattened projection of the soma or of the entire territory. Mean ± SEM: box, SD: whiskers.

(F) Representative images of lucifer yellow-filled striatal astrocytes in either WT or R6/2 mice.

(G) Volume of dorsolateral striatal astrocytes as assessed by 3D reconstructions of the astrocyte somata or territory in WT or R6/2 mice from images such as in (F). Mean ± SEM: box, SD: whiskers.

(H) Cartoon showing that we microinjected AAVs for NAPA-n into either the motor cortex or thalamus, with NAPA-a microinjected into the striatum. Using this approach, we studied spatial interactions of corticostriatal and thalamostriatal inputs with astrocytes in WT and R6/2 mice.

(I and J) The scatter graphs plot areas of colocalization and FRET in WT and R6/2 mice. Mean ± SEM: box, SD: whiskers.

optical readouts that NAPA provides. Second, NAPA could be used as a metric to determine how astrocyte-derived synaptogenic factors regulate distinct classes of synapses within an astrocyte's territory. Third, NAPA could also be used to determine how astrocyte-synapse interactions change in the context of injury, trauma, and disease either during early-stage dysfunctions like those we report for HD model mice, or during strong astrogliosis such as during stroke, neuroinflammation, and spinal cord injury. Fourth, NAPA will be valuable to assess how hIPSC-derived astrocytes, which are being exploited therapeutically, are wired into neural circuits in the context of rescue and repair strategies (Han et al., 2013). Fifth, NAPA will reveal how astrocyte-synapse interactions change in the sleep-wake cycle (Bellesi et al., 2015). Sixth, NAPA provides an optical assay to explore the molecular basis for how astrocytes elaborate their highly complex shapes in relation to specific synapse types, including in the context of gliomas and their associated cognitive deficits (Lin et al., 2017). Seventh, NAPA provides a valuable optical assay to explore how neurons drive complex astrocyte morphology through contact-mediated mechanisms (Stogsdill et al., 2017). Eighth, NAPA is compatible with *in vivo* imaging in awake behaving mice and could be deployed in cortical brain structures for this purpose. Finally, NAPA will permit exploration of the spatial interactions that fine astrocyte processes make with microglial processes in relation to synapses (Schafer et al., 2013). NAPA adds to the toolbox required to understand astrocyte biology within adult neural circuits.

STAR★METHODS

Detailed methods are provided in the online version of this paper and include the following:

- KEY RESOURCES TABLE
- CONTACT FOR REAGENT AND RESOURCE SHARING
- EXPERIMENTAL MODEL AND SUBJECT DETAILS
  - Mouse models
- METHODS DETAILS
  - Molecular biology: plasmid and adeno-associated virus (AAV) generation
  - Cell cultures: transfection and imaging
  - Serial block face scanning electron microscopy (SBF-SEM)
  - Surgery and *in vivo* microinjections of AAV 2/5
  - Brain slice preparation and electrophysiology
  - Electrical stimulation of cortical inputs
  - Oxygen glucose deprivation (OGD)
  - Immunohistochemical (IHC) evaluations
  - Intracellular lucifer yellow dye filling and astrocyte 3D reconstructions
  - Chemicals
- QUANTIFICATION AND STATISTICAL ANALYSIS
  - FRET analyses
  - Measurements of colocalization areas
  - Imaging dynamic changes in astrocyte-synaptic contacts
  - General analyses
- DATA AND SOFTWARE AVAILABILITY

SUPPLEMENTAL INFORMATION

Supplemental Information includes eight figures and two movies and can be found with this article online at https://doi.org/10.1016/j.neuron.2018.03.003.

A video abstract is available at https://doi.org/10.1016/j.neuron.2018.03.003#mmc5.

ACKNOWLEDGMENTS

Supported by the National Institutes of Health grant MH099559 and MH104069 (B.S.K.). J.C.O. was also supported by a T32 Neural Microcircuits Training Grant (NS058280). H.C. was supported by an NIH F30 Training Fellowship (MH106197). S.L.B. was supported by an NIH F31 Training Fellowship (MH107210). Thanks to Dr. M.V. Sofroniew for sharing equipment. Thanks to Dr. M. Levine and C. Cepeda for sharing reporter mice. Thanks to Dr. R. Srinivasan for discussions on FRET. H.C. belongs to the Medical Scientist Training Program and to the NSIDP PhD Program at UCLA. Many thanks to Emily Benson (Renovo Neural) for discussions and guidance on SBF-SEM.

AUTHOR CONTRIBUTIONS

J.C.O. performed the molecular biology, stereotaxic injections, imaging, electrophysiology, and data analyses. H.C. and J.C.O. performed and analyzed the electron microscopy. R.J. performed lucifer yellow iontophoresis and GFAP immunohistochemistry. S.L.B., J.C.O., and K.C.M. performed hippocampal mixed primary culture experiments. B.S.K. conceived the approach, helped analyze data, directed the experiments, assembled the figures, and wrote the paper with help from J.C.O. All authors contributed to the final version.

DECLARATION OF INTERESTS

The authors declare no competing interests.

Received: September 15, 2017
Revised: January 21, 2018
Accepted: March 2, 2018
Published: April 4, 2018

REFERENCES

Ade, K.K., Wan, Y., Chen, M., Gloss, B., and Calakos, N. (2011). An improved BAC transgenic fluorescent reporter line for sensitive and specific identification of striatonigral medium spiny neurons. Front. Syst. Neurosci. *5*, 32.

Allen, N.J., and Eroglu, C. (2017). Cell Biology of Astrocyte-Synapse Interactions. Neuron *96*, 697–708.

Atasoy, D., Aponte, Y., Su, H.H., and Sternson, S.M. (2008). A FLEX switch targets Channelrhodopsin-2 to multiple cell types for imaging and long-range circuit mapping. J. Neurosci. *28*, 7025–7030.

Bazargani, N., and Attwell, D. (2016). Astrocyte calcium signaling: the third wave. Nat. Neurosci. *19*, 182–189.

Bellesi, M., de Vivo, L., Tononi, G., and Cirelli, C. (2015). Effects of sleep and wake on astrocytes: clues from molecular and ultrastructural studies. BMC Biol. *13*, 66.

Bernardinelli, Y., Randall, J., Janett, E., Nikonenko, I., König, S., Jones, E.V., Flores, C.E., Murai, K.K., Bochet, C.G., Holtmaat, A., and Muller, D. (2014). Activity-dependent structural plasticity of perisynaptic astrocytic domains promotes excitatory synapse stability. Curr. Biol. *24*, 1679–1688.

Berney, C., and Danuser, G. (2003). FRET or no FRET: a quantitative comparison. Biophys. J. *84*, 3992–4010.

Bushong, E.A., Martone, M.E., Jones, Y.Z., and Ellisman, M.H. (2002). Protoplasmic astrocytes in CA1 stratum radiatum occupy separate anatomical domains. J. Neurosci. *22*, 183–192.

Bushong, E.A., Martone, M.E., and Ellisman, M.H. (2004). Maturation of astrocyte morphology and the establishment of astrocyte domains during postnatal hippocampal development. Int. J. Dev. Neurosci. *22*, 73–86.

Cahoy, J.D., Emery, B., Kaushal, A., Foo, L.C., Zamanian, J.L., Christopherson, K.S., Xing, Y., Lubischer, J.L., Krieg, P.A., Krupenko, S.A., et al. (2008). A transcriptome database for astrocytes, neurons, and oligodendrocytes: a new resource for understanding brain development and function. J. Neurosci. *28*, 264–278.

Chai, H., Diaz-Castro, B., Shigetomi, E., Monte, E., Octeau, J.C., Yu, X., Cohn, W., Rajendran, P.S., Vondriska, T.M., Whitelegge, J.P., et al. (2017). Neural circuit-specialized astrocytes: transcriptomic, proteomic, morphological, and functional evidence. Neuron *95*, 531–549.e9.

DeFelipe, J., and Jones, E.G. (1988). Cajal on the Cerbral Cortex. An Annotated Translation of the Complete Writings, Chapter 25 (Oxford University Press), p. 481.

Fairless, R., Masius, H., Rohlmann, A., Heupel, K., Ahmad, M., Reissner, C., Dresbach, T., and Missler, M. (2008). Polarized targeting of neurexins to synapses is regulated by their C-terminal sequences. J. Neurosci. *28*, 12969–12981.

Feinberg, E.H., Vanhoven, M.K., Bendesky, A., Wang, G., Fetter, R.D., Shen, K., and Bargmann, C.I. (2008). GFP Reconstitution Across Synaptic Partners (GRASP) defines cell contacts and synapses in living nervous systems. Neuron *57*, 353–363.

Fiala, J.C. (2005). Reconstruct: a free editor for serial microscopy. J Microsc. *218*, 52–61.

Frotscher, M., Studer, D., Graber, W., Chai, X., Nestel, S., and Zhao, S. (2014). Fine structure of synapses on dendritic spines. Front. Neuroanat. *8*, 94.

Gong, S., Doughty, M., Harbaugh, C.R., Cummins, A., Hatten, M.E., Heintz, N., and Gerfen, C.R. (2007). Targeting Cre recombinase to specific neuron populations with bacterial artificial chromosome constructs. J. Neurosci. *27*, 9817–9823.

Gordon, G.W., Berry, G., Liang, X.H., Levine, B., and Herman, B. (1998). Quantitative fluorescence resonance energy transfer measurements using fluorescence microscopy. Biophys. J. *74*, 2702–2713.

Gray, E.G. (1959). Axo-somatic and axo-dendritic synapses of the cerebral cortex: an electron microscope study. J. Anat. *93*, 420–433.

Graybiel, A.M. (2008). Habits, rituals, and the evaluative brain. Annu. Rev. Neurosci. *31*, 359–387.

Graybiel, A.M., and Grafton, S.T. (2015). The striatum: where skills and habits meet. Cold Spring Harb. Perspect. Biol. *7*, a021691.

Grecco, H.E., and Verveer, P.J. (2011). FRET in cell biology: still shining in the age of super-resolution? ChemPhysChem *12*, 484–490.

Haber, M., Zhou, L., and Murai, K.K. (2006). Cooperative astrocyte and dendritic spine dynamics at hippocampal excitatory synapses. J. Neurosci. *26*, 8881–8891.

Halassa, M.M., Fellin, T., Takano, H., Dong, J.H., and Haydon, P.G. (2007). Synaptic islands defined by the territory of a single astrocyte. J. Neurosci. *27*, 6473–6477.

Hama, K., Arii, T., Katayama, E., Marton, M., and Ellisman, M.H. (2004). Tridimensional morphometric analysis of astrocytic processes with high voltage electron microscopy of thick Golgi preparations. J. Neurocytol. *33*, 277–285.

Han, X., Chen, M., Wang, F., Windrem, M., Wang, S., Shanz, S., Xu, Q., Oberheim, N.A., Bekar, L., Betstadt, S., et al. (2013). Forebrain engraftment by human glial progenitor cells enhances synaptic plasticity and learning in adult mice. Cell Stem Cell *12*, 342–353.

Haustein, M.D., Kracun, S., Lu, X.H., Shih, T., Jackson-Weaver, O., Tong, X., Xu, J., Yang, X.W., O'Dell, T.J., Marvin, J.S., et al. (2014). Conditions and constraints for astrocyte calcium signaling in the hippocampal mossy fiber pathway. Neuron *82*, 413–429.

Jiang, R., Haustein, M.D., Sofroniew, M.V., and Khakh, B.S. (2014). Imaging intracellular Ca^{2+} signals in striatal astrocytes from adult mice using genetically-encoded calcium indicators. J. Vis. Exp. *93*, e51972.

Jiang, R., Diaz-Castro, B., Looger, L.L., and Khakh, B.S. (2016). Dysfunctional calcium and glutamate signaling in striatal astrocytes from Huntington's disease model mice. J. Neurosci. *36*, 3453–3470.

Kasthuri, N., Hayworth, K.J., Berger, D.R., Schalek, R.L., Conchello, J.A., Knowles-Barley, S., Lee, D., Vázquez-Reina, A., Kaynig, V., Jones, T.R., et al. (2015). Saturated reconstruction of a volume of neocortex. Cell *162*, 648–661.

Kenworthy, A.K. (2001). Imaging protein-protein interactions using fluorescence resonance energy transfer microscopy. Methods *24*, 289–296.

Khakh, B.S., and Sofroniew, M.V. (2015). Diversity of astrocyte functions and phenotypes in neural circuits. Nat. Neurosci. *18*, 942–952.

Khakh, B.S., Fisher, J.A., Nashmi, R., Bowser, D.N., and Lester, H.A. (2005). An angstrom scale interaction between plasma membrane ATP-gated P2X2 and alpha4beta2 nicotinic channels measured with fluorescence resonance energy transfer and total internal reflection fluorescence microscopy. J. Neurosci. *25*, 6911–6920.

Khakh, B.S., Beaumont, V., Cachope, R., Munoz-Sanjuan, I., Goldman, S.A., and Grantyn, R. (2017). Unravelling and exploiting astrocyte dysfunction in Huntington's disease. Trends Neurosci. *40*, 422–437.

Kim, J., Zhao, T., Petralia, R.S., Yu, Y., Peng, H., Myers, E., and Magee, J.C. (2011). mGRASP enables mapping mammalian synaptic connectivity with light microscopy. Nat. Methods *9*, 96–102.

Kosaka, T., and Hama, K. (1986). Three-dimensional structure of astrocytes in the rat dentate gyrus. J. Comp. Neurol. *249*, 242–260.

Lakowicz, J.R. (2006). Principles of Fluorescence Spectroscopy (Springer).

Lin, C.C., Yu, K., Hatcher, A., Huang, T.W., Lee, H.K., Carlson, J., Weston, M.C., Chen, F., Zhang, Y., Zhu, W., et al. (2017). Identification of diverse astrocyte populations and their malignant analogs. Nat. Neurosci. *20*, 396–405.

Livet, J., Weissman, T.A., Kang, H., Draft, R.W., Lu, J., Bennis, R.A., Sanes, J.R., and Lichtman, J.W. (2007). Transgenic strategies for combinatorial expression of fluorescent proteins in the nervous system. Nature *450*, 56–62.

Manders, E.M.M., Verbeek, F.J., and Aten, J.A. (1993). Measurement of co-localization of objects in dual-colour confocal images. J. Microsc. *169*, 375–382.

Mangiarini, L., Sathasivam, K., Seller, M., Cozens, B., Harper, A., Hetherington, C., Lawton, M., Trottier, Y., Lehrach, H., Davies, S.W., and Bates, G.P. (1996). Exon 1 of the HD gene with an expanded CAG repeat is sufficient to cause a progressive neurological phenotype in transgenic mice. Cell *87*, 493–506.

Martell, J.D., Yamagata, M., Deerinck, T.J., Phan, S., Kwa, C.G., Ellisman, M.H., Sanes, J.R., and Ting, A.Y. (2016). A split horseradish peroxidase for the detection of intercellular protein-protein interactions and sensitive visualization of synapses. Nat. Biotechnol. *34*, 774–780.

Martín, R., Bajo-Grañeras, R., Moratalla, R., Perea, G., and Araque, A. (2015). Circuit-specific signaling in astrocyte-neuron networks in basal ganglia pathways. Science *349*, 730–734.

Marvin, J.S., Borghuis, B.G., Tian, L., Cichon, J., Harnett, M.T., Akerboom, J., Gordus, A., Renninger, S.L., Chen, T.W., Bargmann, C.I., et al. (2013). An optimized fluorescent probe for visualizing glutamate neurotransmission. Nat. Methods *10*, 162–170.

Mori, S. (1966). Some observations on the fine structure of the corpus striatum of the rat brain. Z. Zellforsch. Mikrosk. Anat. *70*, 461–488.

Moss, J., and Bolam, J.P. (2008). A dopaminergic axon lattice in the striatum and its relationship with cortical and thalamic terminals. J. Neurosci. *28*, 11221–11230.

Moss, F.J., Imoukhuede, P.I., Scott, K., Hu, J., Jankowsky, J.L., Quick, M.W., and Lester, H.A. (2009). GABA transporter function, oligomerization state, and anchoring: correlates with subcellularly resolved FRET. J. Gen. Physiol. *134*, 489–521.

Nimmerjahn, A., and Bergles, D.E. (2015). Large-scale recording of astrocyte activity. Curr. Opin. Neurobiol. *32*, 95–106.

Oliet, S.H., Piet, R., and Poulain, D.A. (2001). Control of glutamate clearance and synaptic efficacy by glial coverage of neurons. Science *292*, 923–926.

Reeves, A.M., Shigetomi, E., and Khakh, B.S. (2011). Bulk loading of calcium indicator dyes to study astrocyte physiology: key limitations and improvements using morphological maps. J. Neurosci. *31*, 9353–9358.

Richler, E., Chaumont, S., Shigetomi, E., Sagasti, A., and Khakh, B.S. (2008). Tracking transmitter-gated P2X cation channel activation in vitro and in vivo. Nat. Methods *5*, 87–93.

Schafer, D.P., Lehrman, E.K., and Stevens, B. (2013). The "quad-partite" synapse: microglia-synapse interactions in the developing and mature CNS. Glia *61*, 24–36.

Shigetomi, E., Kracun, S., and Khakh, B.S. (2010). Monitoring astrocyte calcium microdomains with improved membrane targeted GCaMP reporters. Neuron Glia Biol. *6*, 183–191.

Shigetomi, E., Bushong, E.A., Haustein, M.D., Tong, X., Jackson-Weaver, O., Kracun, S., Xu, J., Sofroniew, M.V., Ellisman, M.H., and Khakh, B.S. (2013). Imaging calcium microdomains within entire astrocyte territories and endfeet with GCaMPs expressed using adeno-associated viruses. J. Gen. Physiol. *141*, 633–647.

Shigetomi, E., Patel, S., and Khakh, B.S. (2016). Probing the complexities of astrocyte calcium signaling. Trends Cell Biol. *26*, 300–312.

Son, C.D., Moss, F.J., Cohen, B.N., and Lester, H.A. (2009). Nicotine normalizes intracellular subunit stoichiometry of nicotinic receptors carrying mutations linked to autosomal dominant nocturnal frontal lobe epilepsy. Mol. Pharmacol. *75*, 1137–1148.

Srinivasan, R., Pantoja, R., Moss, F.J., Mackey, E.D., Son, C.D., Miwa, J., and Lester, H.A. (2011). Nicotine up-regulates alpha4beta2 nicotinic receptors and ER exit sites via stoichiometry-dependent chaperoning. J. Gen. Physiol. *137*, 59–79.

Srinivasan, R., Richards, C.I., Dilworth, C., Moss, F.J., Dougherty, D.A., and Lester, H.A. (2012). Förster resonance energy transfer (FRET) correlates of altered subunit stoichiometry in cys-loop receptors, exemplified by nicotinic $\alpha4\beta2$. Int. J. Mol. Sci. *13*, 10022–10040.

Srinivasan, R., Lu, T.-Y., Chai, H., Xu, J., Huang, B.S., Golshani, P., Coppola, G., and Khakh, B.S. (2016). New Transgenic Mouse Lines for Selectively Targeting Astrocytes and Studying Calcium Signals in Astrocyte Processes In Situ and In Vivo. Neuron *92*, 1181–1195.

Stogsdill, J.A., Ramirez, J., Liu, D., Kim, Y.H., Baldwin, K.T., Enustun, E., Ejikeme, T., Ji, R.R., and Eroglu, C. (2017). Astrocytic neuroligins control astrocyte morphogenesis and synaptogenesis. Nature *551*, 192–197.

Stryer, L. (1978). Fluorescence energy transfer as a spectroscopic ruler. Annu. Rev. Biochem. *47*, 819–846.

Sun, W., McConnell, E., Pare, J.F., Xu, Q., Chen, M., Peng, W., Lovatt, D., Han, X., Smith, Y., and Nedergaard, M. (2013). Glutamate-dependent neuroglial calcium signaling differs between young and adult brain. Science *339*, 197–200.

Theodosis, D.T., Montagnese, C., Rodriguez, F., Vincent, J.D., and Poulain, D.A. (1986). Oxytocin induces morphological plasticity in the adult hypothalamo-neurohypophysial system. Nature *322*, 738–740.

Thibault, D., Loustalot, F., Fortin, G.M., Bourque, M.J., and Trudeau, L.É. (2013). Evaluation of D1 and D2 dopamine receptor segregation in the developing striatum using BAC transgenic mice. PLoS ONE *8*, e67219.

Tong, X., Ao, Y., Faas, G.C., Nwaobi, S.E., Xu, J., Haustein, M.D., Anderson, M.A., Mody, I., Olsen, M.L., Sofroniew, M.V., and Khakh, B.S. (2014). Astrocyte Kir4.1 ion channel deficits contribute to neuronal dysfunction in Huntington's disease model mice. Nat. Neurosci. *17*, 694–703.

Ventura, R., and Harris, K.M. (1999). Three-dimensional relationships between hippocampal synapses and astrocytes. J. Neurosci. *19*, 6897–6906.

Volterra, A., Liaudet, N., and Savtchouk, I. (2014). Astrocyte Ca^{2+} signalling: an unexpected complexity. Nat. Rev. Neurosci. *15*, 327–335.

Wilhelmsson, U., Bushong, E.A., Price, D.L., Smarr, B.L., Phung, V., Terada, M., Ellisman, M.H., and Pekny, M. (2006). Redefining the concept of reactive astrocytes as cells that remain within their unique domains upon reaction to injury. Proc. Natl. Acad. Sci. USA *103*, 17513–17518.

Witcher, M.R., Kirov, S.A., and Harris, K.M. (2007). Plasticity of perisynaptic astroglia during synaptogenesis in the mature rat hippocampus. Glia *55*, 13–23.

Wouters, F.S., Bastiaens, P.I., Wirtz, K.W., and Jovin, T.M. (1998). FRET microscopy demonstrates molecular association of non-specific lipid transfer protein (nsL-TP) with fatty acid oxidation enzymes in peroxisomes. EMBO J. *17*, 7179–7189.

Zal, T., and Gascoigne, N.R. (2004). Photobleaching-corrected FRET efficiency imaging of live cells. Biophys. J. *86*, 3923–3939.

STAR★METHODS

KEY RESOURCES TABLE

REAGENT or RESOURCE	SOURCE	IDENTIFIER
Antibodies		
Chicken anti-GFP	Abcam	Cat# ab13970; RRID: AB_300798
Rabbit anti-GFP	Molecular Probes	Cat# A11122; RRID: AB_221569
Mouse anti-NeuN (clone A60)	Millipore	Cat# MAB377; RRID: AB_2298772
Rabbit anti-NeuN	Cell Signaling	Cat# 12943; RRID: AB_2630395
Mouse anti-mCherry	St. John's	Cat#STJ97087; RRID: AB_2687534
Rabbit anti-dsRed	Clontech Laboratories	Cat# 632496; RRID: AB_10013483
Rabbit anti-RFP	Rockland	Cat# 600-401-379; RRID: AB_2209751
Rabbit anti-S100β	Abcam	Cat# ab41548; RRID: AB_956280
Chicken anti-GFAP	Abcam	Cat# ab4674; RRID: AB_304558
Mouse anti-μ-crystallin	Santa Cruz	Cat# sc-376687; RRID: AB_11150103
Alexa goat anti-rabbit 488	Molecular Probes	Cat# A11008; RRID: AB_143165
Alexa goat anti-chicken 488	Molecular Probes	Cat# A11039; RRID: AB_142924
Streptavidin conjugated Alexa 488	Molecular Probes	Cat# S32354; RRID: AB_2315383
Alexa goat anti-rabbit 546	Molecular Probes	Cat#A11010; RRID: AB_143156
Alexa goat anti-mouse 546	Molecular Probes	Cat#A11003; RRID: AB_141370
Alexa goat anti-guinea pig 546	Molecular Probes	Cat#A11074; RRID: AB_2534118
Alexa goat anti-guinea pig 488	Molecular Probes	Cat# A-11073; RRID: AB_142018
Rabbit anti-synaptophysin	Dako	Cat# A0010; RRID: AB_2315411
Mouse anti-MAP2	Abcam	Cat# ab11267; RRID: AB_297885
Guinea pig anti-vGLUT1	Millipore	Cat# MAB5502; RRID: AB_262185
Guinea pig anti-vGLUT2	Millipore	Cat# AB2251; RRID: AB_1587626
Mouse anti-Tyrosine hydroxylase	ImmunoStar	Cat# 22941; RRID: AB_572268
Bacterial and Virus Strains		
AAV2/5 GfaABC$_1$D NAPA-a SV40	This manuscript, UPenn Vector Core	Available upon request from UPenn
AAV2/1 hSynapsin1 NAPA-n SV40	This manuscript, UPenn Vector Core	Available upon request from UPenn
AAV2/1 hSynapsin1 FLEX NAPA-n SV40	This manuscript, UPenn Vector Core	Available upon request from UPenn
AAV2/5 GfaABC$_1$D iGluSnFR SV40	Haustein et al., 2014; UPenn Vector Core	Cat# AV-5-PV4618
AAV2/5 GfaABC$_1$D tdTomato SV40	Shigetomi et al., 2016; UPenn Vector Core	Cat# AV-5-PV3106
AAV2/5 GfaABC$_1$D Lck-GFP SV40	Shigetomi et al., 2013; UPenn Vector Core	Cat# AV-5-PV2369
Chemicals, Peptides, and Recombinant Proteins		
Paraformaldehyde, EM grade	EMS	Cat# 19202
Sodium cadodylate	EMS	Cat# 12300
Glutaraldehyde	Polysciences	Cat# 1909
TTX	Cayman Chemical Company	Cat# 14964
TFB-TBOA	Tocris	Cat# 2532
Phenylephrine	Tocris	Cat# 2838
LY354740	Tocris	Cat# 3246
Lucifer yellow dilithium salt	Sigma-Aldrich	Cat# L0259
Normal goat serum	Vector	Cat# S-1000
Biocytin	Tocris	Cat#3349
Sodium Azide	Sigma	Cat# S2002
Effectene transfection reagent	QIAGEN	Cat# 301425

(*Continued on next page*)

Continued		
REAGENT or RESOURCE	SOURCE	IDENTIFIER
DMEM/F12 GlutaMAX	GIBCO	Cat# 10-565-018
Penicillin/Streptomycin solution	Sigma	Cat# P0781
ImmPACT DAB peroxidase substrate	Vector	Cat# SK-4105
Sodium borohydride	Sigma	Cat# 480886
Critical Commercial Assays		
QIAquick PCR Purification Kit	QIAGEN	Cat# 28104
QIAGEN Mini kit	QIAGEN	Cat# 27104
QIAGEN Endofree MAXI kit	QIAGEN	Cat# 12362
QIAquick Gel extraction Kit	QIAGEN	Cat# 28704
M.O.M. Immunodetection Kit	Vector	Cat# PK-2200
Experimental Models: Cell Lines		
HEK293T Cells	ATCC	Cat# CRL-3216
Experimental Models: Organisms/Strains		
Mouse: R6/2 Huntington's disease model mice	Jackson Labs	JAX Stock # 006494; RRID: IMSR_JAX:006494
Mouse: C57BL/6NJ inbred mice	Jackson Labs	JAX Stock # 005304; RRID: IMSR_JAX:005304
Mouse: D1 Cre mice	MMRRC	Strain # B6.FVB(Cg)-Tg(Drd1-cre)EY262Gsat/Mmucd; RRID: MMRRC_030989-UCD
Mouse: D2 Cre mice	MMRRC	Strain # B6.FVB(Cg)-Tg(Adora2a-cre)KG139Gsat/Mmucd; RRID: MMRRC_036158-UCD
Mouse: D2 eGFP reporter mice	MMRRC	Strain # Tg(Drd2-EGFP)S118Gsat/Mmnc; RRID: MMRRC_000230-UNC
Mouse: D1 tdTomato reporter mice	MMRRC	Strain # B6.Cg-Tg(Drd1a-tdTomato)6Calak/J; RRID: IMSR_JAX:016204
Mouse: *Aldh1l1*-CreERT2 × Lck-GCaMP6f	Srinivasan et al., 2016; Jackson Labs	JAX Stock # 029655; RRID: IMSR_JAX:029655 JAX Stock # 029626; RRID: IMSR_JAX:029626
Recombinant DNA		
pcDNA 3.1 CMV NAPA-a BGH	This manuscript; Addgene	Plasmid # 92277
pcDNA 3.1 CMV NAPA-n BGH	This manuscript; Addgene	Plasmid # 92278
pcDNA 3.1 CMV mCherry-eGFP BGH	This manuscript; Addgene	Plasmid # 92279
pZac 2.1 GfaABC$_1$D NAPA-a SV40	This manuscript; Addgene	Plasmid # 92281
pZac 2.1 GfaABC$_1$D NAPA-a2 SV40	This manuscript	N/A
pZac 2.1 hSynapsin1 NAPA-n SV40	This manuscript; Addgene	Plasmid # 92282
pZac 2.1 hSynapsin1 FLEX NAPA-n SV40	This manuscript; Addgene	Plasmid # 92283
pZac 2.1 hSynapsin1 NAPA-n2 SV40	This manuscript; Addgene	Plasmid # 97212
Software and Algorithms		
OriginPro 8.5/9/2015	Origin Lab	N/A
GraphPad Instat 3	GraphPad Software	N/A
pCLAMP10	Molecular Devices	N/A
ClampFit 10.5	Molecular Devices	N/A
Fluoview FV3000	Olympus	N/A
ImageJ v1.30	ImageJ	N/A
Imaris version 7.6.5	Bitplane	N/A
Reconstruct software version 1.1	Fiala, 2005	https://synapseweb.clm.utexas.edu/software-0

CONTACT FOR REAGENT AND RESOURCE SHARING

Further information and requests for resources and reagents should be directed to and will be fulfilled by the Lead Contact, Baljit S. Khakh (bkhakh@mednet.ucla.edu).

EXPERIMENTAL MODEL AND SUBJECT DETAILS

All mouse experiments were conducted in accordance with the National Institute of Health Guide for the Care and Use of Laboratory Animals and were approved by the Chancellor's Animal Research Committee at the University of California Los Angeles. Mice were housed with food and water available *ad libitum* in a 12 hr light/dark environment. Mice were healthy with no obvious abnormal behavioral phenotype, were not involved in previous studies, and were sacrificed during the light cycle. Both male and female mice were used for experiments (between 8-12 weeks of age).

Mouse models

Most experiments were conducted on C57BL/6N mice (from Taconic) from an in-house colony. Hemizygous R6/2 and non-carrier control WT littermate mice were obtained from Jackson Laboratories (strain B6CBA-Tg(HDexon1)62Gpb/1J; stock #006494). When R6/2 mice were used, the control was always the non-carrier littermates, which we refer to as WT in the text and figures. In other cases when R6/2 mice were not used (e.g., much of the initial validation work), WT mice were C57BL/6N. In order to selectively label subpopulations of MSNs in the striatum we used two BAC reporter lines, which have been shown to selectively label direct (D1) or indirect (D2) pathway MSNs (obtained from Michael Levine). We also used BAC-Cre lines to label these same MSNs with Cre-dependent (FLEX) AAVs, which were maintained in an in-house colony. The BAC-Cre mice were produced by the GENSAT project and were acquired from the Mutant Mouse Resource and Research Center at UC Davis (MMRRC). To label direct pathway MSNs we used the Drd1a-tdTomato reporter line (Strain # B6.Cg-Tg(Drd1a-tdTomato)6Calak/J) or the C57BL/6J congenic Drd1a-Cre line EY262 (Strain # B6.FVB(Cg)-Tg(Drd1-cre)EY262Gsat/Mmucd, MMRRC Stock # 030989-UCD). To label indirect pathway MSNs we used the Drd2-eGFP reporter line which were backcrossed to C57Bl6 (Strain # Tg(Drd2-EGFP)S118Gsat/Mmnc) or the C57BL/6J congenic A2a-Cre line KG139 (Strain # B6.FVB(Cg)-Tg(Adora2a-cre)KG139Gsat/Mmucd, MMRRC stock # 036158-UCD). Mice selectively expressing Lck-GCaMP6f in astrocytes were generated as described previously by crossing *Aldh1l1*-CreERT2 BAC (B6N.FVB-Tg(Aldh1l1-cre/ERT2)1Khakh/J, JAX Stock # 029655) mice with *ROSA26* knockin floxed Lck-GCaMP6f (C57BL/6N-*Gt(ROSA)26Sor*$^{tm1(CAG-GCaMP6f)Khakh}$/J, JAX Stock # 029626) and injecting mice with 75 mg/kg tamoxifen dissolved in corn oil IP for 5 days at 6 weeks of age (Srinivasan et al., 2016).

METHODS DETAILS

Molecular biology: plasmid and adeno-associated virus (AAV) generation

All plasmid constructs were generated using standard molecular biology techniques and the In-Fusion HD Cloning Kit (Clontech). All constructs were sequenced before use and are listed in Figure S1. Three plasmid constructs for cultured cells (CMV NAPA-a BGH, CMV NAPA-n BGH, CMV mCherry-GFP BGH) were generated and subsequently tested in HEK293 cells. These constructs were all cloned into unique HindIII and *XbaI* (mCherry-GFP) or *NotI* (NAPA constructs) restriction sites, downstream of the CMV promoter into pcDNA3.1. In the NAPA-A construct, we used the PDGFR transmembrane domain (Marvin et al., 2013) (Addgene Plasmid #41732). We based our design of the NAPA-n construct on pAAV-CAG-premGRASP-mCerulean (Kim et al., 2011)(Addgene plasmid #34910) where spGFP11 domain (AA32-58) was removed and replaced with cDNA encoding full-length mCherry. The design and 21 residue linker (SSMTGGQQMGRDLYDDDDKDP) of the mCherry-GFP tandem fusion construct was based on the tandem fusion construct Clover-mRuby2 (Addgene plasmid # 49089). The plasmid constructs CMV GFP SV40 and CMV Lck-GFP SV40 have been published previously by us (Shigetomi et al., 2010). For AAV plasmids, we used previously described protocols (Shigetomi et al., 2013). For all constructs, we modified plasmid pZac2.1 GfaABC$_1$D Lck-GCaMP3 (Addgene plasmid # 44330). Briefly, we generated adeno-associated virus plasmids (AAV2/5 for astrocyte targeted AAVs or 2/1 for neuronal targeted AAVs) capable of expressing the selected cDNAs using the following strategy. For these plasmids, GfaABC$_1$D NAPA-a SV40 and GfaABC$_1$D NAPA-a2 SV40, we removed Lck-GCaMP3 using *Xho1* and *Xba1* restriction enzymes and infused the NAPA-a constructs. For NAPA-a2, GFP was removed from NAPA-a and replaced with cDNA for mNeonGreen (Allele Biotechnology). For plasmid hSynapsin1 NAPA-n SV40 we removed both the promoter (GfaABC$_1$D) and the Lck-GCaMP3 cDNA and cloned in the hSynapsinI promoter (Addgene plasmid # 51085) and NAPA-n. For NAPA-n2, mCherry cDNA was removed and replaced with cDNA of mScarlet (Addgene plasmid # 85042). We also created a Cre-dependent (FLEX) expression vector from hSynapsin1 NAPA-n SV40 by removing the NAPA-n cDNA and replacing it with a unique *Spe1* restriction site flanked by 5′ lox2272/loxP and 3′ lox2272/loxP sites (Addgene plasmid # 18925) creating a multipurpose shuttle vector called "hSynapsin1 FLEX SV40." We then infused NAPA-n in an inverted orientation using the open *SpeI* site, creating the final vector hSynapsin1 FLEX NAPA-n SV40. The fully sequenced "pZac2.1" plasmids were sent to the Penn Vector Core, which used them to generate AAV serotypes 2/5 or 2/1 for each construct yielding a concentration of $\sim$1 × 10^{13} genome copies/ml (gc/mL). All of our constructs have been deposited at Addgene in the Khakh lab repository, and the AAVs are available from the UPenn Vector Core Catalog.

Cell cultures: transfection and imaging

Human embryonic kidney cells (HEK293, ATCC) were grown in DMEM/F12 + Glutamax (GIBCO) supplemented with fetal bovine serum (10% v/v), penicillin (100 units/mL) and streptomycin sulfate (100 μg/mL). Cells were grown in a humidified atmosphere of 95% air/5% CO_2 at 37°C in a cell culture incubator. The cells were split 1 in 10 when confluence reached 60%–90%, which was

generally every 3 to 4 days. Cells were prepared for transfection by plating onto six-well plates at the time of splitting ~2 days before transfection at 60%–70% confluence. For transient expression in HEK293, we used 0.5–1 μg plasmid cDNA per ~10^6 cells. Constructs were transiently transfected using Effectene transfection reagent (QIAGEN) according to the manufacturer's instructions. Total transfected DNA was maintained between groups by co-transfecting empty plasmid vector pcDNA 3.1 (Life Technologies). Transfected cells were plated on poly-l-lysine coated coverslips.

For primary culture experiments, mouse hippocampi were dissected from newborn (P0) mice and physically dissociated by triturating before plating on poly-DL-lysine (1 mg/mL) coated coverslips (Carolina Biologicals, Burlington, NC) at a density of ~80,000 cells/well. Neurons were cultured at 37°C in a 5% CO_2 incubator in Neurobasal A medium (Invitrogen, Carlsbad, CA), supplemented with β-mercaptoethanol (Sigma, St. Louis, MO), monosodium glutamate (Sigma), GlutaMAX (Invitrogen), and B27 (Invitrogen). Neurons were transfected at 9-12 DIV using $CaPO_3$; briefly, 3 μg of DNA was incubated with calcium and HEPES-phosphate buffer before adding directly to cultured neurons, then removed and washed 3x with conditioned media before allowing cells to express plasmid in conditioned media overnight (16 hr). Astrocytes were transfected using a modified Lipofectamine protocol wherein plasmid DNA was incubated with Lipofectamine 2000 (Invitrogen) according the manufacturer's instructions and applied directly to cultured cells for 5-6 hr before removal and allowing overnight (16 hr) expression. Coverslips were then washed quickly with PBS, fixed for 10 min in para-formaldehyde (Electron Microscopy Sciences, Hatfield, PA), permeabilized with 0.1% Triton X-100 (Fisher), stained with primary and secondary antibodies, and mounted onto slides with Aqua Polymount (Polysciences, Inc Warrington, WA) and imaged.

For HEK293 cell experiments, coverslips were removed from DMEM/F12 media 40-64 hr post transfection, rinsed twice with HEK293 cells imaging buffer (composition in mM: 150 NaCl, 1 $CaCl_2$, 1 $MgCl_2$, 10 glucose, 10 HEPES, pH 7.4 with NaOH) and placed into continuously perfused recording baths. The cells were then imaged at 1 Hz using a 40x water objective (Olympus) LUMPlanFLN-W 0.80 NA. For acid quenching experiments, imaging was started while cells were in pH 7.4 buffer and the perfusate was then switched to pH 3.5 while continuously imaging. We only analyzed the fluorescent signals of those cells that showed a stable position throughout the time-series (no movement greater than 3–4 μm in any axis). Any small movements in cell position were corrected by using stack registration (TurboReg Plugin) in ImageJ. For these HEK293 cell experiments, we used the 488 nm wavelength of an Argon laser to excite eGFP, with the intensity adjusted to 2%–5% of the maximum output (10 mW). The emitted light path consisted of a band-pass emission filter (505–525 nm) before the photomultiplier tube. The constructs containing mCherry was excited by the 543 nm wavelength of a HeNeG laser at 4%–10% of the maximum output (1 mW). The emitted light pathway consisted of a dichroic mirror (SDM560, Olympus) and a 560–600 nm band-pass emission filter feeding into the photomultiplier tube.

Serial block face scanning electron microscopy (SBF-SEM)

Excitatory synapses

For serial block face scanning electron microscopy (SBF-SEM) we used outbred Swiss-Webster mice (Taconic, P59-P64; 2 males, 1 female). They were euthanized with 200 mg/kg pentobarbital and transcardially perfused with 60 mL of fixative solution (4% paraformaldehyde [EMS #19202]) and 2.5% glutaraldehyde (Polysciences #1909) in a 0.1 M sodium cacodylate (EMS #12300) buffer, pH 7.2). Brains were sliced into 1 mm coronal sections, and we then further dissected the dorsal lateral striatum. Tissues were post-fixed in fixative solution for 48 hr post euthanasia at 4°C. Fixed tissues were preincubated with 0.1% tannic acid, and then stained with osmium-ferrocyanide, followed by tetracarbohydrazide treatment, and then further stained with 2% aqueous osmium tetroxide. Samples were then incubated overnight in saturated aqueous uranyl acetate, followed by Walton's lead aspartate stain. Next, samples were dehydrated through a series of alcohol solutions, followed by propylene oxide, a 50/50 propylene oxide and resin mixture, before being embedded in Epon 812-substitute resin. The resin blocks were then trimmed and mounted on an aluminum pin, coated with colloidal silver paste around the block edges, and then examined in a Zeiss Sigma VP system equipped with a Gatan 3View in-chamber ultramicrotome stage with low-kV backscattered electron detectors optimized for 3View systems. Samples were imaged at 2.25 kV, at 6.8 nm/pixel resolution, with field sizes between 40–50 μm in *x-y* and slice thickness of 80 nm. The acquisition of the EM data was performed by Renovo Neural (Cleveland, Ohio). Image series were registered and then analyzed using Reconstruct software version 1.1 (https://synapseweb.clm.utexas.edu/software-0). These image series were used in our previous study, but were reanalyzed here for our purposes (Chai et al., 2017). For this study, excitatory asymmetric spines on striatal medium spiny neuron (MSN) dendrites were traced. Striatal MSNs have aspinous primary dendrites that become spiny upon branching. Only dendrites whose aspiny primary and spiny secondary or tertiary portions found in the image series were analyzed. At least three dendrites were analyzed per mouse and all excitatory spines on selected dendrites were analyzed. Presynaptic axon boutons were traced along with the postsynaptic density and nearby astrocyte processes. Postsynaptic and presynaptic membranes were defined by the presence of the PSD on the spine and the opposing membrane on axon boutons, respectively. Astrocyte processes were identified by their persistent irregular shape through multiple sections and by the presence of glycogen granules. The shortest line between the presynaptic or postsynaptic membranes and nearest astrocyte process was measured for traced synapses using the "Distance" function in Reconstruct software. As the lower resolution limit was 6.8 nm in the X-y axis, we imposed this cutoff for distance measurements. The quality of the raw data was assessed by Emily Benson, an experienced electron microscopist at Renovo Neural (Cleveland, Ohio). The traced structures were independently assessed and agreed on by two investigators (JCO and HC), before measurements were made.

Tyrosine hydroxylase positive putative dopaminergic terminals and synapses

For SBF-SEM we used inbred C57BL/6NJ mice (Jackson Labs, P56-P63; 1 males, 2 females). They were euthanized with 200 mg/kg pentobarbital and transcardially perfused with 5 mL of PBS followed by 60 mL of light fixative solution (4% paraformaldehyde EMS #19202) and 0.1% glutaraldehyde (Polysciences #1909) in a 0.1 M PBS buffer, pH 7.2). Following fixation, the carcasses were allow to post-fix for 1 hr. The brains were removed from the carcasses and incubated in sodium borohydride solution (1% sodium borohydride, PBS) to quench free fixative and then sliced into 100 μm thick coronal sections after setting brains into 4% agarose blocks. For immunohistochemistry, tissue sections were rinsed in PBS to remove agarose and then the endogenous peroxidase activity was quenched by the addition of 1% H_2O_2 in PBS with 0.3% NGS for 5 min and then triple rinsed with PBS to remove the excess peroxide. The sections were then antigen blocked for 1 hr (Vector #PK-2200) and then placed into primary antibody solution (1:750 mouse anti-TH (Immunostar) 10% NGS, PBS) for 48 hr with gentle rocking. After primary incubation, samples were triple washed for 5 min each in PBS and incubated in biotinylated goat anti-rabbit secondary antibody (1:200) for 90 min. Slices were then washed three times for 5 min in PBS and then incubated in avidin/biotin complex solution (Vector #PK-2200) for 90 min, made according to the manufacturer's instructions. The slices were then washed in TBS (Tris buffered saline, 50 mM Tris base, 137 mM NaCl, pH 7.6) three times for 5 min each and then incubated for 1 min in freshly made and filtered DAB solution (Vector #SK-4105 in TBS) while watching the reaction solution darken. The slices were then washed four times with TBS for 5 min each to quench the DAB reaction and remove unreacted products.

The stained sections were immediately placed into EM fixative solution (4% paraformaldehyde) and 2.5% glutaraldehyde in a 0.1 M sodium cadodylate buffer, pH 7.2) for 48 hr at 4°C. Fixed tissues were preincubated with 0.1% tannic acid, and then stained with osmium-ferrocyanide, followed by tetracarbohydrazide treatment, and then further stained with 2% aqueous osmium tetroxide. Samples were then incubated overnight in saturated aqueous uranyl acetate, followed by Walton's lead aspartate stain. Next, samples were dehydrated using a graded series of ethanol, followed by propylene oxide, prior to an overnight incubation in 50% propylene oxide and 50% resin mixture on a rotator. The samples were moved to 100% resin for 90 min prior to embedding in Epon 812-substitute resin within a silicone mold for 48 hr at 60°C. The resin blocks were then trimmed and mounted on an aluminum pin, and exposed tissue edges were coated with colloidal silver liquid. After the silver is dried, the samples were examined in a Zeiss Sigma VP system equipped with a Gatan 3View in-chamber ultramicrotome stage with low-kV backscattered electron detectors optimized for 3View systems. Samples were imaged at 2.25 kV, at 6.8 nm/pixel resolution, with field sizes between 40-50 μm in x-y and slice thickness of 80 nm. The acquisition of the EM data was performed by Renovo Neural (Cleveland, Ohio). Image series were registered and then analyzed using Reconstruct software version 1.1 (https://synapseweb.clm.utexas.edu/software-0).

TH positive axons on the tissue face were tracked into deeper sections and traced. At least four TH axons were analyzed per mouse. TH axospinal synapses and the most proximal astrocyte processes were traced. Unlike typical symmetrical synapses, dopaminergic synapses do not have a widened synaptic cleft, frequently appear as "transient," and have little observable synaptic specializations (Gray, 1959; Mori, 1966; Moss and Bolam, 2008). Dopaminergic terminals were identified by enlargement of axon diameter and the presence of vesicles in the TH positive terminals. Spines were identified and postsynaptic membranes traced. Presynaptic membranes were defined by the opposing membrane on dopaminergic terminal boutons. Astrocyte processes were identified by their irregular shapes through multiple sections and by the presence of intracellular glycogen granules (i.e., as above for excitatory synapses). Once the relevant structures were traced, the measurements were performed identically to that for excitatory synapses. The shortest vector between the presynaptic and postsynaptic membranes and nearby astrocyte processes was measured for each traced synapse using the "Distance" function in Reconstruct software. As the resolution was 6.8 nm in our quantified scans in the X-y axis, we imposed this as the lower cutoff for distances. The quality of the raw data was assessed by Emily Benson, an experienced electron microscopist at Renovo Neural (Cleveland, Ohio). The traced structures were independently assessed and agreed on by two investigators (CO and HC), before measurements were made.

Surgery and *in vivo* microinjections of AAV 2/5

The detailed AAV microinjection protocol for striatum has been described previously (Jiang et al., 2016; Tong et al., 2014). Male and female P42 –P56 C57BL/6N, hemizygous R6/2, or non-carrier WT mice were used in all experiments. Briefly, animals were deeply anesthetized using isoflurane (induction at 5%, maintenance at 1%–2.5% v/v). After induction of anesthesia, the mouse's head was gently placed into a stereotaxic frame and secured by blunt ear bars and their noses were placed into an anesthesia system (David Kopf Instruments). Mice were administered 0.05 mL of buprenorphine (Buprenex, 0.1 mg/mL) subcutaneously before surgery. The incision site was then sterilized three times with 10% povidone iodine and 70% ethanol. Short (5-8 mm) skin incisions were made, followed by craniotomies 2–3 mm in diameter above the injection site using a small steel burr (Fine Science Tools) powered by a highspeed drill (K.1070; Foredom). Saline (0.9%) was occasionally applied onto the skull to reduce heating caused by drilling. Unilateral viral injections were performed by using a stereotaxic apparatus (David Kopf Instruments) to guide the placement of beveled glass pipettes (1B100 – 4; World Precision Instruments) into the appropriate brain region. Our stereotaxic coordinates (Axes: Anterior-Posterior / Medial-Lateral / Dorsal-Central; relative to Bregma) for AAV microinjection were as follows: dorsolateral striatum: +0.8 / +2.0 / −2.4, motor cortex: −0.1 /+0.7 / −0.3, rostral intralamminar nucleus of the thalamus: −1.4 / +0.6 / −3.1, substantia nigra pars compacta: −3.0 / + 1.5 /−4.2. In this study, the following viruses and their titers were used: AAV2/5 GfaABC$_1$D NAPA-a (1.85 × 10^{13} gc/mL), AAV2/5 GfaABC$_1$D Lck-GFP (2.4 × 10^{13} gc/mL), AAV2/5 GfaABC$_1$D tdTomato (5.0 × 10^{13} gc/mL), AAV2/1 hSynapsin1 NAPA-n (6.7 × 10^{12} gc/mL), AAV2/1 hSynapsin1 FLEX NAPA-n (1.5 × 10^{13} gc/mL) and AAV2/5 GfaABC1D

iGluSnFR (4.2×10^{12} gc/mL). For experiments involving two viruses, we injected volumes of each virus to maintain an approximately equivalent titer of each (0.5-1.2 μL per virus) and this was injected by using a syringe pump at 200 nL/min (Pump11 PicoPlus Elite; Harvard Apparatus). No more than 2 μL of AAV was injected in any one animal. Glass needles were left in place for at least 10 min. For the experiments in the cortex and thalamus of control and HD model mice, we took care to microinject AAV NAPA-n at coordinates more distal to the striatum (and at lower volumes), to ensure AAV did not spread to the striatum. Incisions were sutured with single external 6 – 0 nylon sutures. After surgery, animals were allowed to recover overnight in cages placed halfway on a low-voltage heating pad. Subcutaneous buprenorphine was administered twice daily for 2 days after surgery. In addition, trimethoprim/sulfadiazine diet (275 and 1,365 ppm, TD.06596, Teklad) was fed *ad lib* after surgery. After recovering from surgery, the mice were sacrificed 20–25 days later for imaging experiments.

Brain slice preparation and electrophysiology

Striatal slices were prepared from P70 WT and R6/2 mice. Briefly, animals were deeply anesthetized and decapitated. The brains were placed in ice-cold modified artificial CSF (aCSF, containing in mM: 194 sucrose, 30 NaCl, 4.5 KCl, 1 $MgCl_2$, 26 $NaHCO_3$, 1.2 NaH_2PO_4, and 10 D-glucose) and cut into 300 μm-thick coronal or parasagittal slices containing the striatum and cortex. Brain slices were allowed to equilibrate for ~30 min at 32–34°C in normal aCSF (containing in mM; 124 NaCl, 4.5 KCl, 2 $CaCl_2$, 1 $MgCl_2$, 26 $NaHCO_3$, 1.2 NaH_2PO_4, and 10 D-glucose) continuously bubbled with a mixture of 95% O_2/5% CO_2, stored at room temperature in the same buffer, and used for experiments within ~6 hr of slicing.

Electrophysiological methods were described previously (Jiang et al., 2016; Tong et al., 2014). Cells were visualized with infrared optics on an upright microscope (BX61WI, Olympus). pCLAMP9 software and a MultiClamp 700B amplifier was used for electrophysiology (Molecular Devices). For striatal astrocyte recordings, the aCSF contained the following (in mM): 124 NaCl, 4.5 KCl, 2 $CaCl_2$, 1 $MgCl_2$, 26 $NaHCO_3$, 1.2 NaH_2PO_4, and 10 D-glucose continuously bubbled with a mixture of 95% O_2/5% CO_2. For these recordings, the intracellular solution in the patch pipette contained the following (in mM): 135 potassium gluconate, 3 KCl, 0.1 $CaCl_2$, 10 HEPES, 1 EGTA, 8 Na_2-phosphocreatine, 4 Mg-ATP, 0.3 Na_2-GTP, pH 7.3 adjusted with KOH. For biocytin labeling, 2 mg/ml biocytin was dissolved in the intracellular solution. For these recordings, the patch-pipette tip resistance was 4-6 MΩ. The initial access resistances was <20 MΩ for all cells; if this changed by >20% the cell was discarded.

Electrical stimulation of cortical inputs

For stimulation of cortical axons, we applied electrical field stimulation (EFS) using a bipolar matrix electrode (FHC) that was placed at the dorsolateral corpus callosum to evoke glutamate release (Jiang et al., 2016). The astrocytes or neurons to be assessed were typically located 200 μm away from the stimulation site. For Lck-GCaMP6f or iGluSnFR imaging of Ca^{2+} and glutamate, individual pulses were 0.2 ms in duration and stimuli were delivered at 4 mA and at 10 Hz. iGluSnFR imaging was performed at 0.5-1 Hz based on past work, which shows EFS-evoked glutamate signals can be measured and are prolonged when glutamate uptake was blocked. iGluSnFR itself has intrinsically fast kinetics in solution that we and others have modeled (Haustein et al., 2014; Marvin et al., 2013), but this should not be confused with the kinetics of the underlying EFS-evoked glutamate signals in brain slices which are slower and detected with our methods (Chai et al., 2017; Haustein et al., 2014; Jiang et al., 2016). Electrically evoked EPSCs were analyzed using Clampfit version 10.2 (Molecular Devices).

Oxygen glucose deprivation (OGD)

OGD was induced by superfusing slices with a hypoglycemic, isosmotic aCSF in which the glucose was substituted with 6 mM sucrose, 2 mM 2-deoxyglucose and 3 mM NaN_3 continuously bubbled with a mixture of 95% N_2/5% CO_2. Experimental evaluations were made after about 15 mins of OGD, when the change in MSN and astrocyte membrane potential had reached steady state in preliminary experiments that are reported in the text.

Immunohistochemical (IHC) evaluations

Prior to transcardial perfusion, mice were euthanized with 200 mg/kg pentobarbitol (i.p.). Once reflexes were lost, the abdominal cavity was opened and heparin (0.1 mL, 100 USP) was injected into the heart to prevent blood clotting. The mouse was perfused with 50 mL 0.1 M phosphate buffered saline (PBS) followed by 50 mL 10% buffered formalin (Fisher Scientific). After careful removal from the skull, the brain was post fixed in 10% buffered formalin overnight. The tissue was cryoprotected in phosphate buffered 30% sucrose solution the following day for at least 2 days at 4°C until use. 40 μm sections were prepared using a cryostat microtome (Leica) and processed for immunohistochemistry. To stain for fluorescence microscopy, sections were washed 4 times in 0.1 M PBS for 5 min each, and then incubated in a blocking solution containing 5% NGS in 0.1 M PBS with 0.2% Triton X-100 for 1 hr at room temperature with agitation. Sections were then incubated in primary antibodies diluted in 0.1 M PBS with 5% NGS and 0.2% Triton X-100 overnight at 4°C. The following primary antibodies were used: chicken anti-GFP (1:1000; Abcam Cat# ab13970 RRID: AB_300798), mouse anti-NeuN (1:1000; Abcam Cat# ab104225 RRID: AB_10711153), rabbit anti-NeuN (1:1000; Cell Signaling; RRID: AB_2630395), chicken anti-GFAP (1:500, Abcam Cat# ab4674 RRID: AB_304558), rabbit anti S100β (1:2000, Abcam Cat# ab41548 RRID: AB_956280), rabbit anti-dsRed (1:1000, Clontech Laboratories Cat# 632496 RRID: AB_10013483), mouse anti-mCherry (1:1000, St. John's Cat# STJ97087), guinea pig anti-vGlut1 (1:1000, Millipore Cat# AB2251 RRID: AB_1587626), guinea pig anti-vGlut2 (1:2000, Millipore Cat# AB2251 RRID: AB_1587626), rabbit anti-RFP (1:200, Rockland Cat# 600-401-379

RRID: AB_2209751), streptavidin anti-biotin Alexa 488 conjugate (1:2000, Molecular Probes Cat# S32354 RRID: AB_2315383), mouse anti-tyrosine hydroxylase (1:750, Immunostar, Cat# 22941 RRID: AB_572268), mouse anti-μ-crystallin (1:250, Santa Cruz Biotechnology, Cat# sc-376687 RRID: AB_11150103), Rabbit anti-synaptophysin (1:600, Dako, Cat# A0010 RRID: AB_2315411). The next day the sections were washed 4 times in 0.1 M PBS for 5 min each before incubation at room temperature for 1–2 hr with secondary antibodies diluted in 0.1 M PBS with 5% NGS and 0.2% Triton X-100. The following Alexa conjugated secondary antibodies were used: goat anti-chicken 488 (1:1000, Molecular Probes Cat# A-11039 RRID: AB_142924), goat anti-guinea pig (1:1000, Molecular Probes Cat# A-11073 RRID: AB_142018), goat anti-rabbit 546 (1:1000, Molecular Probes Cat# A-11035 RRID: AB_143051), goat anti-guinea pig 546 (1:1000, Thermo Fisher Scientific Cat# A-11074 RRID: AB_2534118) and goat anti-mouse 546 (1:1000, Molecular Probes Cat# A-11030 RRID: AB_144695). The sections were then rinsed 4 times in 0.1 M PBS for 5 min, and briefly dipped in diH_2O before being mounted, dried, and coverslipped on microscope slides. Fluorescence images were taken using UPlanSApo 20X 0.85 NA and UPlanFL 40X 1.30 NA oil immersion objective lens and FV1000 Fluoview confocal laser-scanning microscope. We used the 488 nm wavelength of an Argon laser to excite Alexa488, with the intensity adjusted to 0.5%–5% of the maximum output, which was 10 mW. The emitted light path consisted of a band-pass emission filter (505–525 nm) before the photomultiplier tube. Alexa 546 was excited by the 543 wavelength of a HeNe laser at 5%–30% of the maximum output (1 mW). The emitted light pathway consisted of a dichroic mirror (SDM560, Olympus) and a 560–600 nm band-pass emission filter.

Intracellular lucifer yellow dye filling and astrocyte 3D reconstructions

Our astrocyte dye filling protocol has been adapted from past work (Bushong et al., 2002; Chai et al., 2017). Mice were euthanized with pentobarbitol (i.p.). After loss of reflexes, the chest cavity was opened and the mice were transcardially perfused by 40 mL Ringer's solution (composition in mM: 135 NaCl, 5 KCl, 15 $NaHCO_3$, 1.25 $NaHPO_4$, 1 $MgCl_2$, 2 $CaCl_2$, 11 Dextrose and 0.02% lidocaine) which was warmed to 35°C and bubbled for 30 min with a mixture of 95% O_2/5% CO_2. Mice were then perfused by fixative solution (10% buffered formalin), decapitated and the brains were then gently removed and placed into fixative solution at RT for 1 hr. The brains were then washed and gently rinsed 3 times in 0.1 M phosphate buffered saline for 5 min each. 120 μm coronal sections were then taken. Sharp, high resistance microelectrodes were then pulled and backfilled with 1%–2.5% di lithium lucifer yellow CH solution. Striatal astrocytes were identified by their small (10 μm), round cell bodies and lack of large cellular processes. Lucifer yellow was injected into the cells by injecting current of a few nanoamperes generated by a Current Isolator (Model A365, WPI). After injection, the confocal stacks of the cell were collected with a z step size of 0.25 μm. Following dye filling, confocal z stacks were immediately taken and cell reconstructions were processed offline using Imaris 7.6.5 (Bitplane, South Windsor, CT, USA). Briefly, a three-step reconstruction strategy was used. First, the soma was rendered by setting a high threshold of the light intensity with the Local Contrast method (i.e., remove the rest of the cell other than the soma as background). Then, we masked the rendered soma using the Mask function. Second, primary branches, defined as the branches emanating from the soma, were isolated and rendered by setting an appropriate intermediate threshold. The primary branches were masked similarly. Lastly, the rest of the cell was rendered by setting a low threshold value. The 3D surface rendering of astrocytes for calculating the territory volume was achieved similarly, utilizing background subtraction function within Imaris. An appropriate threshold using "Absolute Intensity" method was set to subtract background noise to generate a closed surface covering the entire cell. The volumes for all the renderings were obtained through the Statistics function within Imaris.

Chemicals

All general chemicals used were from VWR, Tocris, Alomone or Sigma. Other specific reagents and kits are listed in the methods.

QUANTIFICATION AND STATISTICAL ANALYSIS

FRET analyses

We measured FRET by two independent techniques: donor dequenching (DD) and sensitized emission (SE). The methods for pixel-by-pixel FRET from sensitized emission and donor dequenching have been described in detail (Moss et al., 2009; Richler et al., 2008; Son et al., 2009; Srinivasan et al., 2011). For cell culture experiments, FRET was examined 40–64 hr after transfection, while for experiments in acute slices FRET was examined 18–22 days following AAV injections *in vivo*.

The excitation wavelength used for NAPA-a or GFP was 488 nm, and fluorescence was detected at 505–525 nm ($Image_G$), while for NAPA-n or mCherry the excitation wavelength was 543 nm and fluorescence was detected at 560–600 nm ($Image_C$). For SE experiments, we measured an additional component, which is the total signal emitted at 560–600 nm when excited at 488 nm ($Image_F$). The photomultiplier voltages, gains, offsets, scan speeds, and pinhole diameters were constant for all similar experiments (cultured cells or brain tissue). During image acquisition, the focal plane was adjusted to between 15 and 30 μm beneath the surface of the slice or at the widest diameter of the imaged cell. In the cell culture experiments using SE, cells transfected with CMV mCherry or eGFP were included in every imaging session. For similar experiments in brain slices, control animals were injected with either NAPA-a or NAPA-n AAVs to determine spectral bleed through in slices.

We determined FRET efficiency for DD experiments in a cell by stepwise photobleaching of NAPA-n or mCherry using 543 nm wavelength laser light in 2 min increments. Only those cells that showed no changes in morphology were analyzed. We quantified the average change in GFP and mCherry fluorescence across all photobleaching steps and plotted increased GFP fluorescence

versus the decrease in mCherry fluorescence. We calculated FRET efficiency from these plots for each ROI by determining the slope of the line using linear regression. We calculated FRET efficiency according to the following formula where I_{DA} represents the pixel intensity (I) of GFP in the presence of mCherry and I_D represents GFP emission intensity after mCherry was photobleached.

$$E_{DD} = 1 - \frac{I_{DA}}{I_D} \quad \text{(Equation 1)}$$

For calculation of FRET by SE we assessed FRET efficiency by subtracting donor bleedthrough and acceptor crosstalk from the $Image_F$ series. This subtraction is necessary, because there are three components that contribute to the apparent FRET image. First, the emission of GFP detected at 560–600 nm, i.e., the donor bleed through coefficient, BT_D, multiplied by the pixel intensity of GFP in the $Image_G$ series, I_D. Second, direct excitation of mCherry at 488 nm, i.e., the acceptor crosstalk coefficient, BT_A, multiplied by the pixel intensity of mCherry in $Image_C$ series, I_A. Third, the FRET component, $I_{netFRET}$. For all experiments involving calculation of SE. FRET, the PixFRET ImageJ Plug-in was used to determine GFP (BT_D) and mCherry (BT_A) and to calculate the FRET efficiency values at each pixel (Gordon et al., 1998).

$$I_{netFRET} = I_{FRET} - (I_D \times B_{TD}) - (I_A \times BT_A) \quad \text{(Equation 2)}$$

To calculate FRET efficiency from sensitized emission images, we used a method similar to that for acceptor photobleaching experiments where I_{DA} is the fluorescence of the donor in the presence of the acceptor and I_D is the intensity of the donor in the absence of the acceptor (Kenworthy, 2001; Wouters et al., 1998). However, for sensitized emission we used a modification, whereby the intensity of the donor in the absence of the acceptor (I_D) was determined by the addition of I_{DA} and the calculated value, $I_{netFRET}$, which was calculated by determining the additive bleed through components in the above equation (Zal and Gascoigne, 2004). Therefore, we substituted the following into our equation for FRET calculation by donor dequenching:

$$I_D = I_{DA} + I_{netFRET} \quad \text{(Equation 3)}$$

With the background and bleed through components determined, the FRET efficiency value for each pixel was calculated and the data were presented as 32-bit images with the FRET efficiency displayed on a LUT scale. Prior to analysis, we acquired independent images of mCherry and GFP (NAPA-n and NAPA-a) containing samples for bleed through calibration. Images were compiled into donor stacks ($Image_G$, $Image_F$), acceptor stacks (Image$_C$, $Image_F$), and sample image stacks ($Image_G$, $Image_C$, $Image_F$) prior to image processing.

$$E_{SE} = 1 - \frac{I_{DA}}{I_{DA} + I_{netFRET}} \quad \text{(Equation 4)}$$

Using the efficiency values, we then estimated the inter-molecular distance (r) for the mCherry and GFP fusion construct using the Förster equation.

$$E = R_0^6 / \left(R_0^6 + r^6\right) \quad \text{(Equation 5)}$$

In Equation (5), R_0 includes terms for the donor quantum efficiency (φ_D), the solvent refractive index (n), overlap of the donor emission and acceptor absorption spectra (J_{DA}), and the orientation factor (κ^2), which are described using the equation below.

$$R_0^6 = \left(8.79 \times 10^{23}\right)\kappa^2 n^{-4} \varnothing_D J_{DA} \quad \text{(Equation 6)}$$

Importantly, the term for the fluorophore dipole orientation factor (κ^2) at 2/3 assumes random orientations of the FPs, but could range from 0 to 4 depending on the orientation of the fluorophore dipoles as being perpendicular (0) or parallel (4) (Lakowicz, 2006). Given that we do not know the relative orientation of the FPs on astrocyte processes and synapses, assuming a κ^2 value of 2/3 is parsimonious and in accord with past guidance (Grecco and Verveer, 2011; Lakowicz, 2006).

Assuming genuine FRET occurs in a small sub diffraction volume between astrocyte processes and synapses, then additional donor and acceptor fluorophores in the shared confocal volume that do not undergo FRET will arithmetically decrease apparent FRET by their contributions to the intensity terms for I_A or I_D used in Equation 2. This type of "bystander" contribution would occur if, for example, there were bystander donor or acceptor bearing astrocyte processes and terminals, respectively within the imaged volumes. However, FRET is most reliable when the concentration of the donor and acceptor are of the same order of magnitude, i.e., when the donor/acceptor ratios are between 0.1 and 10 (Berney and Danuser, 2003). Such ratios were 2.02 ± 0.05 (1026 ROIs), 1.07 ± 0.03 (939 ROIs), 3.32 ± 0.07 (811 ROIs), and 1.97 ± 0.10 (952 ROIs) for thalamostriatal, nigrostriatal, collateral, and corticostriatal NAPA experiments, respectively (18-23 cells from 4-5 mice in each case). They were thus all within the acceptable range. Furthermore, for our most complete dataset, the average NAPA-n and NAPA-a intensities were 294 ± 12 and 494 ± 11 a.u., respectively for ROIs displaying FRET (n = 965 ROIs from 4 mice). In accord, 87% of the FRET ROIs were within the donor/acceptor ratio range of ~0.1 and ~10, which we interpret to indicate that bystander contributions to our FRET measurements are small for the majority of the data. Of the remaining 13% of ROIs, 3% displayed donor/acceptor ratios >10, and 10% displayed values <0.1, which would lead to over- and under-estimation of FRET efficiency from Equation (2). Interestingly, the NAPA-n and NAPA-a intensities were 237 ± 10 and 603 ± 37 a.u., respectively for equivalently sized ROIs from the same images that did not display FRET, suggesting that the presence or absence of FRET in our measurements was not due to excessively high or low donor or acceptor expression. Overall,

the presence of high amounts of either bystander donors or acceptors is expected to contribute to FRET evaluations, but as far as we can ascertain this condition was not observed in our analysis of ROIs with or without FRET. Similar appropriate assessments will still be needed in future studies on a case-by-case basis and bystander contributions may be more significant for large presynaptic terminals (e.g., mossy fiber boutons) that contain multiple active zones in a terminal with very thin astrocyte processes mostly at the perimeter (Haustein et al., 2014). Such terminals do not exist in the striatum.

Measurements of colocalization areas

We used the Manders' colocalization method for assessment of axon terminals within the territory of an astrocyte (Manders et al., 1993). For these analyses, the images of astrocyte processes and presynaptic terminals were thresholded to remove background signals. Images were then converted to a binary format in which pixels above the threshold were counted as 1 and pixels with signal at the level of background or lower were counted as 0. The thresholded and binary-converted images of the NAPA-n and NAPA-a were then added, resulting in an image of the colocalized signals, which permitted the calculation of the percentage of the astrocyte territory that contained the colocalized signals.

Imaging dynamic changes in astrocyte-synaptic contacts

Dynamic changes in astrocyte synaptic contacts by NAPA were acquired by serial imaging of the sample in the three filter sets ($Image_G$, $Image_C$, $Image_F$). Sample images were then sorted and stacked for post-processing using custom built ImageJ macros. Slow drifts in astrocyte position (2–5 μm) were corrected with the TurboReg Plugin in ImageJ. Astrocyte territory sizes for all experiments were estimated by measuring the area of a region of interest (ROI) that surrounded the largest fluorescence profile of astrocytes from $Image_G$. Once sample images were arranged into individual three-channel stacks the PixFRET ImageJ Plug-in was used to calculate FRET images using the same background settings for all images in the time series. FRET ROI properties were measured within the astrocyte territory, and FRET efficiency and areas were assessed over the time series.

General analyses

Data from every experiment represents a minimum of n animals with a balanced number of male and female mice. In all the imaging experiments, n was >4 mice. In some of the initial testing experiments, n was 3 mice. Sample sizes were not calculated *a priori*. For AAV injections, mice were randomly assigned to each experimental group. No experimental data points were excluded.

Statistical tests were run in Origin 9. Summary data are presented as mean ± SEM. In other cases, box and whisker plots are used. Unless otherwise stated, in these the mean is shown with a circle, the SEM with a box and the SD with whiskers. Note that in some of the graphs, the bars representing the SEM are smaller than the symbols used to represent the mean. For each set of data to be compared, we determined within Origin whether the data were normally distributed or not using the Shapiro-Wilk test. If they were normally distributed, we used parametric tests. If the data were not normally distributed, we used non-parametric tests. Paired and unpaired Student's two-tailed t tests (as appropriate) and two tailed Mann–Whitney tests were used for most statistical analyses with significance declared at $p < 0.05$, but stated in each case with a precise p value. When a statistical test was employed that was not a Student's t test or a Mann-Whitney test for a specific case, then it is stated as such in the text. When the p value was less than 0.0001, it is stated as $p < 0.0001$ to save space on the figure panels and text. If the p value was greater than 0.05, then it is stated as $p > 0.05$. n is defined as the number of cells, regions-of-interest, field-of-view, numbers of separate transfections or numbers of mice throughout on a case-by-case basis depending on the particular experiment. Throughout the manuscript, the results of statistical tests (p values and n numbers) are reported in full on the figure panels to save space in the main body of the manuscript. However, where appropriate key statistics are also reported in the text.

DATA AND SOFTWARE AVAILABILITY

All constructs generated as part of this study will be available from Addgene. Data analyses and software guidance are available upon request.